Department of Physics and Astronomy
Heidelberg University

Bachelor Thesis in Physics
submitted by

Joschka J. Goes

born in Bremen (Germany)

2021

Investigation of Space Charge Effects Inside an Electron Beam Ion Trap using Dielectronic Recombination of Neon

This Bachelor Thesis has been carried out by Joschka Goes at the
Max Planck Institute for Nuclear Physics in Heidelberg
under the supervision of
Prof. José Crespo López-Urrutia

Abstract

Electron Beam Ion Traps are a proven tool for the production and study of highly charged ions. This work presents a systematic measurement of the Dielectronic Recombination of Neon over a continuous range of trap depths and energies at 20 different electron beam currents. This measurement allows for insights into the varying space charge inside the trap and other effects changing the effective electron beam energy. This insight is then used to calculate the electron beam radius, the expected number of ions trapped and the approximate resonance strength of dielectronic recombination.

Zusammenfassung

Electron Beam Ion Traps sind ein ideales Werkzeug zur Produktion und Untersuchung hochgeladener Ionen. In dieser Arbeit wurde eine systematische Messung von dielektronischer Rekombination von Neon über einen kontinuierlichen Bereich von Energien und Fallentiefen für 20 verschiedene Stromstärken angefertigt. Diese Messung bietet Einsichten in die Dynamik der Raumladung in der Falle und andere Einflüsse auf die effektive Elektronenstrahlenergie. Diese Einsicht wird dann verwendet, um den Radius des Elektronenstrahls zu bestimmen und die Anzahl der gefangenen Ionen abzuschätzen. Diese Parameter zusammen mit der Zählrate ermöglichen das Bestimmen des Wirkungsquerschnitts von dielektronische Rekombination in Neon.

Contents

Chapter 1

Introduction

Spectroscopy is one of the greatest tools available to physicists. It got its beginnings with Newton showing that the white light of the sun is made up of a continuous series of colours, later Fraunhofer would discover a number of dark lines in this spectrum unknowingly finding the key to for a better understanding of the structure of atoms and the makeup of the sun. This potential was then realized and formalized by Kirchhoff and Bunsen establishing spectroscopy as a tool for understanding the very small and the astronomically large. Later the insights gathered using spectroscopy would lead to the formulation of some of the most fundamental theories of physics like quantum mechanics and special and general relativity.[15] Today x-ray spectra are captured by satellites like ESAs XMM-Newton to observe faraway places. One thing to observe are highly charged ion (HCI) clouds, they in their process of ionization and recombination emit light with specific wavelengths that give information on their makeup and state, these emissions can be analyzed using spectroscopy[14]. In addition to theoretical explanations, controlled experiments on highly charged ions have to be conducted, to make sense of the observed spectra. Here Electron Beam Ion Traps (EBITs) are the perfect tool, they allow for the breeding of HCIs and can then contain them for further investigation. The phenomena that can be examined include the ionization process the then following recombination processes, photoexcitation and ionization of highly charged ions and many more.

This bachelor thesis aims to investigate the dynamics within such a Trap to better understand the tool itself. Of special interest is the interaction of the space charge of the ions and the electron beam, which have an impact on the kinetic energy of the electron beam and therefore the apparent position of resonant processes like the in this work observed dielectronic recombination (DR). These insights are gained by tracking the nominal beam energy at which the KLL DR resonances of Neon appear when changing both the electric current of the beam and the trap depth. The resulting changes will allow for the estimation parameters like

the electron beam radius and the number of ions trapped, which in turn allows for an approximation of the resonance strength of dielectronic recombination. Notably, the resonance strength determined this way does not rely on any prior knowledge gained through theoretical simulations but is only calculated from the observed quantities in the experimental setup.

This work is structured in three parts, first a theoretical overview of the setup and important physical phenomena, then a more specific description of actual measurement setup and the measurements made, then in the last part the analysis of the acquired data.

Chapter 2

Theory

In this chapter, the basics of an Electron Beam Ion Trap are covered. The first part mostly concerns an outline of the setup. In the second part of the chapter, the main physical processes that dictate the dynamics within the trap are explained.
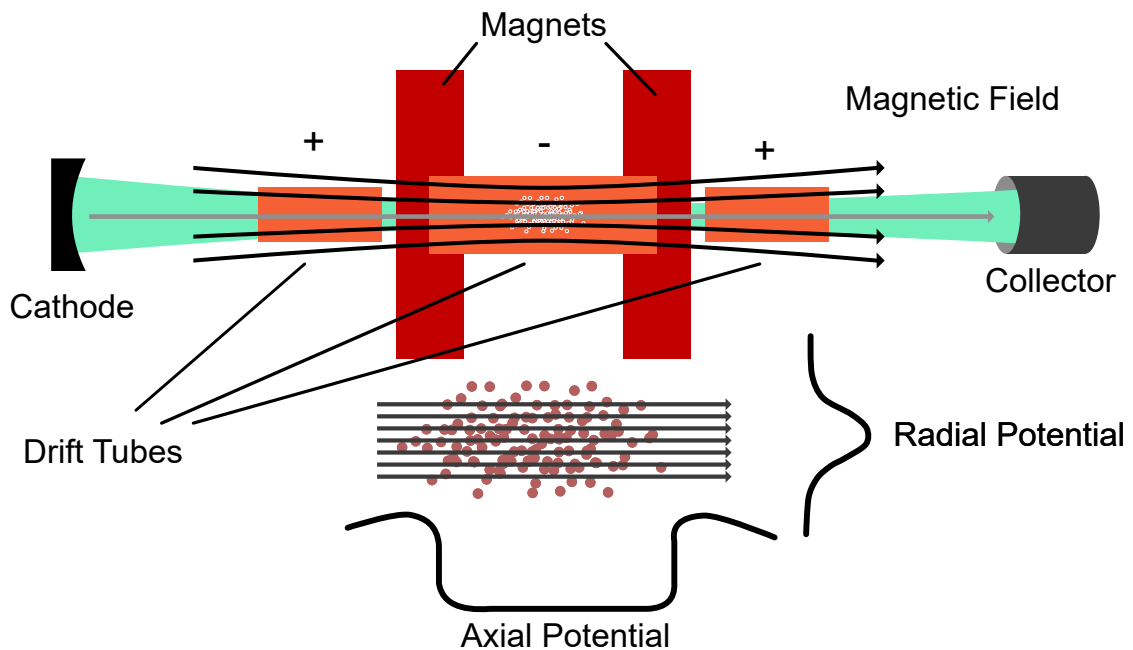
2.1 Electron Beam Ion Trap

Figure 2.1: Schematic sketch of an EBIT, with an rough sketch of the interal potential below.

Electron Beam Ion Traps or short EBITs are traps that allow for the breeding and storing of highly charged ions. Ions are created via electron impact ionization. This is done by creating an electron beam, which is used both for ionizing the ions and for radially trapping them using the resulting space charge. The beam is formed by accelerating the electrons using a series of ring electrodes called the drift tubes. In the centre of the trap, a magnetic field is used to compress the electron beam, which increases the current density and therefore the production rate of ions. The ions get trapped axially by drift tubes around the centre of the trap whose potential can be raised relative to the potential of the centre electrode. Finally, the electrons of the beam are decelerated and collected by the collector [3].

2.1.1   Electron Beam

One of the primary parameters of the elctron beam is its radius only within the electron beam ionization or recombination processes can take place. To describe the Electron Beam radius the Herrmann radius is used, it gives a good prediction of the radius through which 80% of the beam passes.

$$r_H = r_B \sqrt{\frac{1}{2} + \sqrt{\frac{1}{4} + \frac{8 m_e k_B T_c r_c^2}{e^2 B^2 r_B^4} + \frac{B_c^2 r_c^4}{B^2 r_B^4}}} \tag{2.1}$$

Which improves on the Brillouin radius

$$r_B = \sqrt{2 m_e \frac{I_e}{\pi \epsilon_0 v_e e B}} \tag{2.2}$$

Here B is the magnetic field strength at the trap, I_e the current, e the elementary charge, m_e the electron mass, k_B the boltzmann constant, ϵ_0 the vacuum permittivity and v_e the electron velocity. r_c is the cathode radius, kT_c the characteristic electron energy at the cathode and B_c is the magnetic field at the cathode.

The potential of the electron beam is described by the following equation:

$$\phi_e(r \leq r_e) = \frac{I_e}{4\pi\epsilon_0 v_e} \left[\left(\frac{r}{r_e}\right)^2 + ln\left(\frac{r_e}{r_{dt}}\right)^2 - 1 \right] \tag{2.3}$$

$$\phi_e(r \geq r_e) = \frac{I_e}{4\pi\epsilon_0 v_e} ln\left(\frac{r}{r_{dt}}\right)^2 \tag{2.4}$$

Where r_{dt} is the drift tube radius, and r_e the electron beam radius which we approximate by using equation (2.1)[11].

7

The density of the elctron beam can be intresting when calculating the cross section of processes, like ionization or dielectronic recombination. The geometric average of the electron beam density n_e can be calculated using the equation

$$n_e = \frac{I_e}{\pi r_e^2 e v_e} \tag{2.5}$$

Where I_e is the eletron beam current, r_e is the beam radius and v_e is the velocity of the electrons. This velocity can be calculated using the corrected beam energy by rearanging the kinetic energy formula:

$$v = c\sqrt{1 - \left(\frac{m_e c^2}{E + m_e c^2}\right)^2} \tag{2.6}$$

Where c is the speed of light and $E = qU$ is the electron energy determined by the acceleration voltage and the elementary charge. This density inside the electron beam however is not expected to be homogenous and a better model for the radial density distribution might be a Gaussian shape [1].

$$n_e(r) = n_e(0)exp(-\frac{r^2}{r_H^2}ln2) \tag{2.7}$$

2.1.2   Spacial Ion Distribution

For the same reason that the electron density of the electron beam is interesting, the spatial distribution of the ions is important. They are assumed to be distributed according to the Boltzmann distribution. For a given charge state q_i the density is

$$n_{q_i}(r) = n_{q_i}(0)exp(\frac{-eq_i\phi(r)}{kT_{q_i}}) \tag{2.8}$$

The distribution is therefore dependent on the charge-state-specific temperature T_{q_i} and the total electrostatic potential causing a complex interaction between charge states.[3]

2.1.3   Electro Static Reach-Through

The way an EBIT is set up, the different drift tubes are used to accelerate the electron beam and trap the ions. For that function, all the electrodes are driven individually or in pairs around the drift tube in the centre. Although they are individually driven, the actual potential is always dependent on the surrounding electrodes due to their proximity. This means that changes in trap depth - meaning

a change in the potential of the outer drift tubes - always affects the potential of the central drift tube. A change in the potential of the central drift tube directly impacts the electron beam energy. The drift tubes in this experiment are shielded from outward influences of this type but are susceptible to reach-through from each other.

2.1.4 Space Charge Compensation

When the trap fills the positively charged ions start to compensate the space charge of the electron beam. The space charge potential of the ions will be denoted by ϕ_i and the potential of the electron beam has already been discussed in 2.1.1. This causes the observed resonances to shift as the effective electron beam energy changes. Additional shifts towards higher energies are caused by general losses in the setup, like the required work to escape the cathode.

$$\phi_{tot} = \phi_e + \phi_i \tag{2.9}$$

2.2 Ionization Processes

Ionization in general is the process of removing one or more electrons from either a neutral atom or an already ionized atom. Atoms can be ionized by inelastic collision with an electron. If that electron has a kinetic energy higher than the binding energy of the weakest bound electron in the atom, the electron is ejected from the atom leaving the atom ionized. This is called electron impact ionization and is the method of ionization in an EBIT. Atoms can also be ionized using the photoelectric effect. The cross-section of electron impact ionization is smaller for higher charged ions and therefore the production rate gets lower the higher the charge state gets.[3]

$$A^{q+} + e^- \rightarrow A^{(q+1)+} + 2e- \tag{2.10}$$

2.3 Recombination Processes

Inside an Electron Beam Ion Trap ions are, as the name implies, trapped, but an individual ion might escape due to high temperatures or recombine with electrons and 'escape' the trap that way. In the following, the two most relevant of those recombination processes are described, which together with the escape due to high energy determine the distribution of different ion charge states within the trap.

9

2.3.1 Radiative Recombination

Radiative Recombination (RR) is one of the primary ways Ions in an EBIT can lower their charge state. In the process, an electron from the continuum is captured into a bound state of the ion. This is accompanied by the emission of a photon.

$$A^{+(q_i)} + e^- \rightarrow A^{+(q_i-1)} + \hbar\omega \tag{2.11}$$

This is the time reversed process of photon ionization. Energy conservation dictates for the energy of the photon E_γ:

$$E_\gamma = E_{\text{kin}} - E_b \tag{2.12}$$

Where E_{kin} is the kinetic energy of the electron and E_b is the bining energy of the resulting state.

2.3.2 Dielectronic Recombination

Dielectronic recombination (DR) is the inverse process to the Auger process. A free electron is captured, while an already bound electron in the ion is excited. This is a resonant process where the energy of the free electron E_{kin} plus the binding energy of the captured state E_B is equal to the energy required to excite the already bound electron ΔE.

$$\Delta E = E_{\text{kin}} + E_B \tag{2.13}$$

The doubly excited state then decays radiatively. Although it also can auto ionize, in which case we do not speak of dielectronic recombination. The branching ratio between the decay through radiation or the Auger process varies between the specific excited states. The resonances are commonly referred to by the principal quantum numbers of the involved electrons in the excited state. This work looks at KLL dielectronic recombination resonances, meaning that an electron is captured into the L shell, while another electron is lifted from the K to the L shell. [8] There are also higher-order recombination processes that distribute the kinetic energy of the captured electron onto multiple bound electrons, these have generally lower cross-sections and are not covered in this work.

Measuring cross-sections for dielectronic recombination with any energy resolution is difficult due to the resonant nature of dielectronic recombination. Due to that, the resonance strength is a more useful quantity. The DR line s with a cross-section of $\sigma_s(E)$ has per definition the following resonance strength: [17]

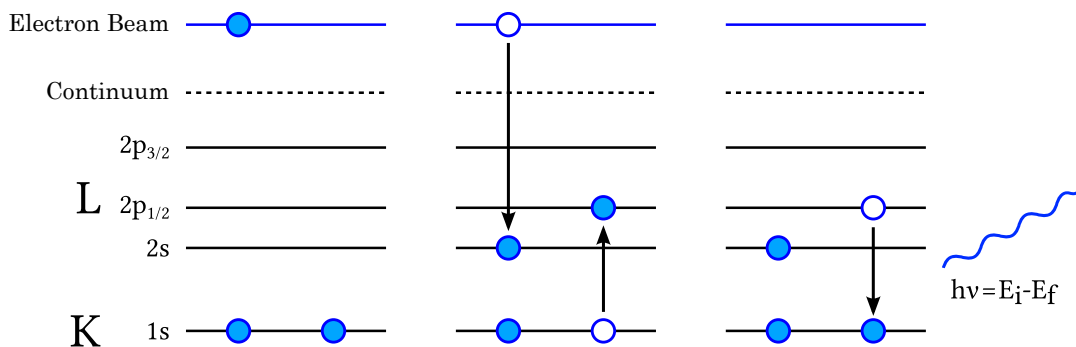$$S_s = \int_0^\infty \sigma_s(E)dE \tag{2.14}$$

10

Figure 2.2: KLL dielectronic recombination of a helium like ion. On the left the initial state is shown, the centre shows the capture process and on the right, the decay of the excited state is shown. In the equation, E_i refers to the energy of the excited state and E_f to the energy of the lower state. h is the plank constant and ν is the frequency of the emitted photon. Image source: [4]

Polarization Effect

Due to the unidirectional nature of the electrons in the electron beam of an EBIT, there is an imbalance in the population of magnetic sublevels in the ion cloud. Due to relativistic effects in electron-electron interaction, this causes linear polarization of the emitted photons, which in turn means that the emission intensity depends on the angle respective to the electron beam. The 4π averaged emitted line intensity I has the following relation to the observed intensity at 90°:

$$I(90°) = \frac{3I}{3-P} \tag{2.15}$$

where P is the polarization of the observed transition.[13, 18]

2.4 Ion Temperature

As already alluded to in Section 2.3, temperature plays a major role in the escape of ions from the trap. The dominant processes in the heating and cooling of ions are electron beam heating (also referred to as Landau-Spitzer heating) and evaporative cooling. Other less important temperature processes include ionization heating.

In an electron beam, heating ions are heated through long-range Coulomb collisions with electrons from the beam. The rate of beam heating is given by:

$$\frac{d}{dt}\left(\frac{3}{2}N_{q_i}k_BT_{q_i}\right)^{\text{Beam}} = f_{e,q_i}N_{q_i}\frac{e^2q_i^2n_e\ln\Lambda_{e,q_i}}{4\pi\epsilon_0^2m_{q_i}v_e} \tag{2.16}$$

11

Here i always referes to a species of ions, like above N_{q_i} is the axial number density, T_{q_i} the temperature of the species. f_{e,q_i} is the electron-ion overlap factor for the specific species and is determined by the following ratio: $\frac{N_{q_i}^{\text{in}}}{N_{q_i}}$ where $N_{q_i}^{\text{in}}$ is the axial ion density only including ions inside the electron beam. Λ_{e,q_i} is the Coulomb logarithm given by $\Lambda_{e,q_i} = \ln(r_{dt}/\langle b_{90°}\rangle)$ with $\langle b_{90°}\rangle = \frac{q_i e}{8\pi\epsilon_0 E_e}$, giving the ratio between the largest possible collision parameter and the mean collision paramter for 90° deflections. Important here is that due to the q_i^2 dependence higher charged ions are heated more than lower charged ions.

Evaporative cooling is a process in which more energetic ions escape the trap lowering the overall ion temperature. Lower charge states escape easier due to the lower repulsion on the outer drift tubes and the decreased temperature in these states is transferred to a higher charge state by ion-ion collisions. This can significantly improve the trapping of ions, which is why light gasses which are rapidly ionized are often injected into the trap to lower the temperature. [3]

Chapter 3

Experimental Setup

3.1 EBIT

In this work, the PolarX-EBIT was used which is one of the Heidelberg compact electron beam ion traps (HC-EBIT). Fundamentally, an EBIT consists of a cathode where the electrons are emitted, a focusing electrode and anode, followed by a series of drift tubes along the beam. After the drift tubes, a collector is catching the electrons. Before and after the central drift tube there are additional drift tubes that can be raised and lowered in potential to axially trap the ions. In the PolarX-EBIT the beam is compressed by a magnetic field created by a set of permanent magnets in a specific arrangement so that a fairly homogenous magnetic field permeates the central drift tube. The PolarX-EBIT also offers an extraction mechanism for the bred ions. Additionally, there is an injection system, to inject the to be examined element, along with possible coolants, into the central drift tube. The inside of the EBIT is evacuated to levels in the low 10^{-9} mbar range so that only a few contaminants appear in the spectra and or change the dynamics within the trap. [12]

3.2 Off-Axis Electron Gun

The PolarX-EBIT is somewhat special in, that it has its electron gun mounted off-axis. This is advantageous when the EBIT is used for experiments involving photoexcitation and photoionization, as it allows for maximum overlap of photons and the trapped ion cloud. This is not used in this experiment but makes it necessary to split the anode into two separate electrodes. The rear anode creates the extraction potential inside the gun. The front anode bends the beam onto the axis of the drift-tube assembly. The presence of the magnetic field also introduces an additional sideways motion for the off-axis electron beam, due to the Lorentz

force which has to be compensated with a split focus electrode. These electrodes are also used to control the emission current, by applying different voltages to the electrodes. [12]

3.3 Drift Tube Assembly

The drift tube assembly consists of stainless steel electrodes that are isolated and held in place by ceramic isolators. The central electrode in which the ions are trapped is 25 mm long and has an inner diameter of 5 mm. It features four 15 mm long openings in the side leaving a radial opening of 70°. To keep the electric Field homogenous despite these openings, the openings are wrapped in a conductive mesh which has an optical transmissivity of over 90%. The two electrodes before and after the trap electrode in the centre of the beam reach slightly into the cavity of the trap electrode so that a direct transition, without interruptions by neutral potentials, is achieved. The two outer drift tubes are 32 mm long and in trumpet-shaped flairs to help with the feeding in of the electron beam.[2]
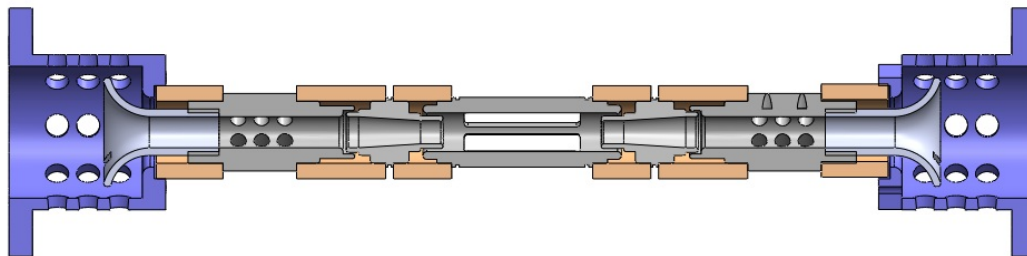

Figure 3.1: The drift tubes of the PolarX-EBIT. The setup features two outer drift tubes with trumpets, two inner drift tubes for changing the trap depth and a center electrode where the ions are trapped within, with cutouts for various detectors. Image source: [2]

3.4 Data Acquisition System

All data of the EBIT is acquired using the MPA4 (multi-parameter data acquisition) system by FAST ComTec. Connected to that system is a range of 13Bit digital to analogue converters with an input range of 0 to 10 Volts. All the ADCs

14

can be run either in SVA (sampling voltage analyzer) or PHA (pulse height analyzer) mode. The different inputs can be set up to record a signal from all inputs if a pulse is detected at a specific input. The data is accumulated into a binary file that contains the ADC data for individual events and a timestamp relative to the start of measurement with 1ms precision. The resulting data can be viewed directly in the MPANT software provided by the manufacturer. The data analysis was done using a custom Python script.

3.5   Measurement scheme

The measurement happens in events, an event is triggered by the detection of a photon. Once a photon is detected the measurement of the beam energy, trap depth and current is triggered. To isolate the KLL-DR resonancies we remove every event outside of the specific photon energy range corresponding to the resonancies in a post-processing step on the data. The events are then accumulated into a 2d-histogram with the beam energy on the x-axis and the trap depth on the y-axis. In this setup, the current is sequentially adjusted in discrete steps and a histogram is created for each current step.

To control the measurements, a Python script programs three function generators with two channels each. First, a sawtooth signal is generated with the desired trap depth cycle frequency. It is added onto one of two identical and in phase oscillating triangle functions that are used to drive the outer and inner drift tubes of the trap, causing the beam energy to periodically rise and fall. The sawtooth signal is added to the signal of the outer drift tubes, this eventually results in a complete scan over all beam energy - trap depth combinations if the periods are an irrational multiple of each other. Since the function generators are not capable to produce the required voltages on their own two amplifiers one for the outer and one for the trap drift tube are used to increase the voltage 400 times over the signal generated by the function generators. The sawtooth signal and a sawtooth signal with the same frequency and in phase with the drift tube signals are directly connected to the MPA-system, along with the photon detector and a signal encoding the measured current. The current is measured at the collector and is then captured by a National Instruments card in the computer and then output again as a voltage in the correct range for the MPA-system. The current is controlled via software using two focus elements for the electron beam. The current is updated only every second or so, which is why the current is only adjusted slowly and in discrete steps, while all other parameters are changed continuously using the signal generators. At the end of each energy cycle, the contents of the trap are dumped for a few milliseconds. This is done by very briefly (400 ns) raising the voltage of the central drift tube.

3.6 X-ray Detector

The setup uses a KETEK VITUS H150 Silicon Drift Detector for detecting photons. It is usually equipped with a 25µm beryllium window, but this has been removed to avoid the resulting photon absorption. The effective detection area of the sensor is 150 mm^2.[6] and the distance from the trap centre is 27.7 ± 0.8 mm.
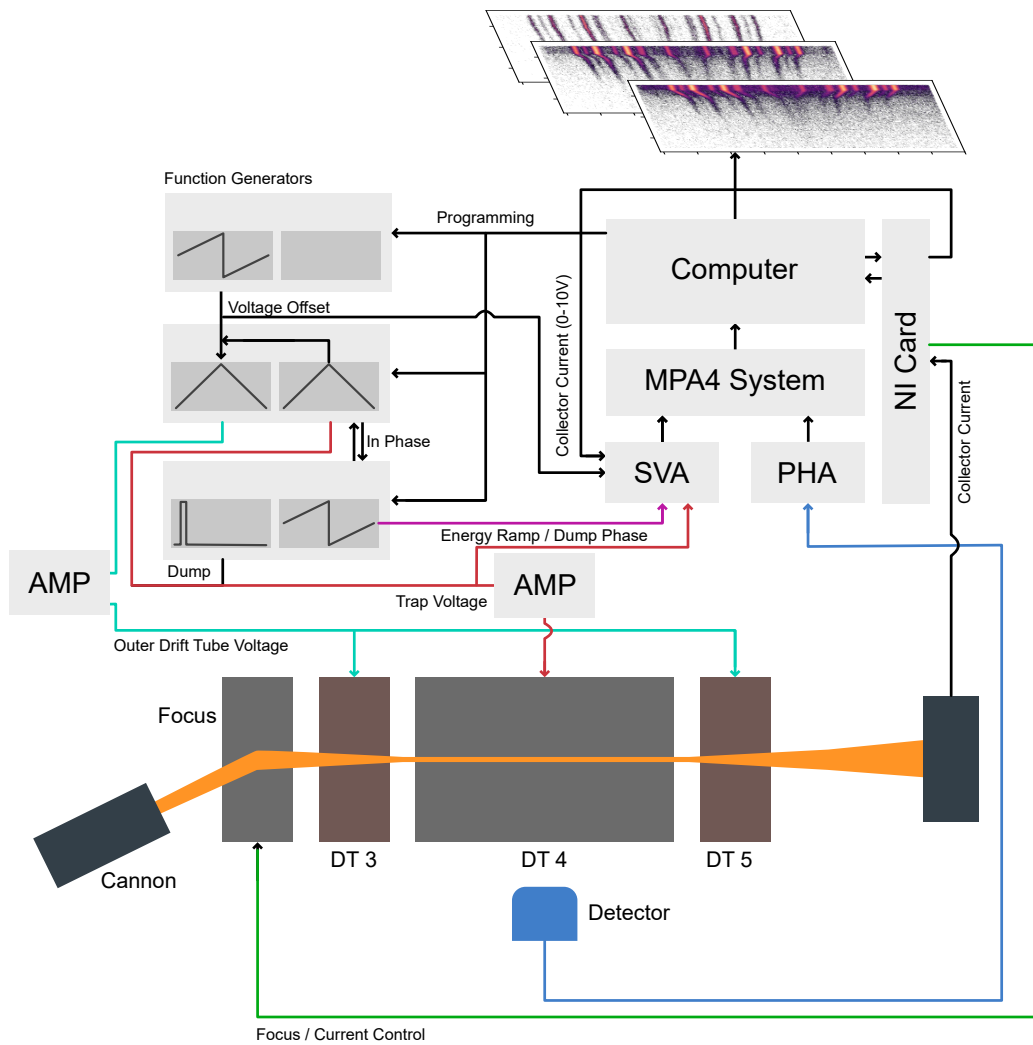
Figure 3.2: Schematic overview of the measurement setup and the control and aquesition scheme.

Chapter 4

Measurement Results and Evaluation

4.1 Overview

Before getting into the analysis of the results I will present a brief overview of the captured data, beginning with a histogram of the captured photon energy vs. the beam energy (See Figure 4.1). In the following analysis, all events outside of the photon energy channels of 3800 to 4500 are discarded. In the next step, trap depth is plotted against the beam energy. Before that makes sense, events have to be grouped into the 20 different current targets. The actual measured current follows a normal distribution around the target value, and events are attributed to the closest target value. The resulting bins are around 75µA wide and the distribution has a standard deviation of approximately 20µA. This bin width impacts the sharpness of the recorded lines as the changing current changes the radial trapping potential. The resulting plots after separating the currents can be seen in Figure 4.2.

Table 4.1: Measurement Settings

Total Time	411878307 ms
Kickduration	400 ns
Energy Ramp Time	2.0 s
Center Drift Tube Minimal Voltage	405 V
Center Drift Tube Maximal Voltage	495 V
Cathode Voltage	249.5 V
Trap Depth Ramp Time	103.1416 s
Minimal Trap Depth	-50 V
Maximal Trap Depth	10 V
Current Ramp Time	100 min
Current Steps	20
Minimal Current	0.5 mA
Maximal Current	2.0 mA
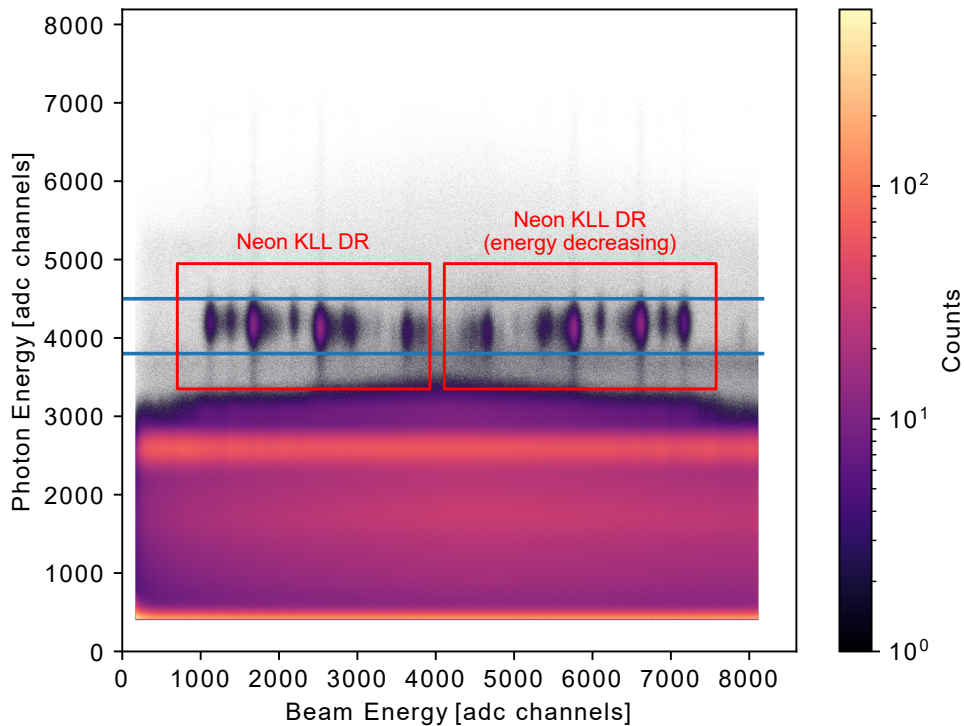
Figure 4.1: Neon KLL resonances in a photon-energy - electron-beam-energy plot. The image is soft as trap depth and the current was varied during capture which changes the space charge present in the trap which in turn changes the effective resonance energy. The beam energy raises from left to right up until the centre from which it decreases again. The blue lines enclose the area where photons are not discarded.
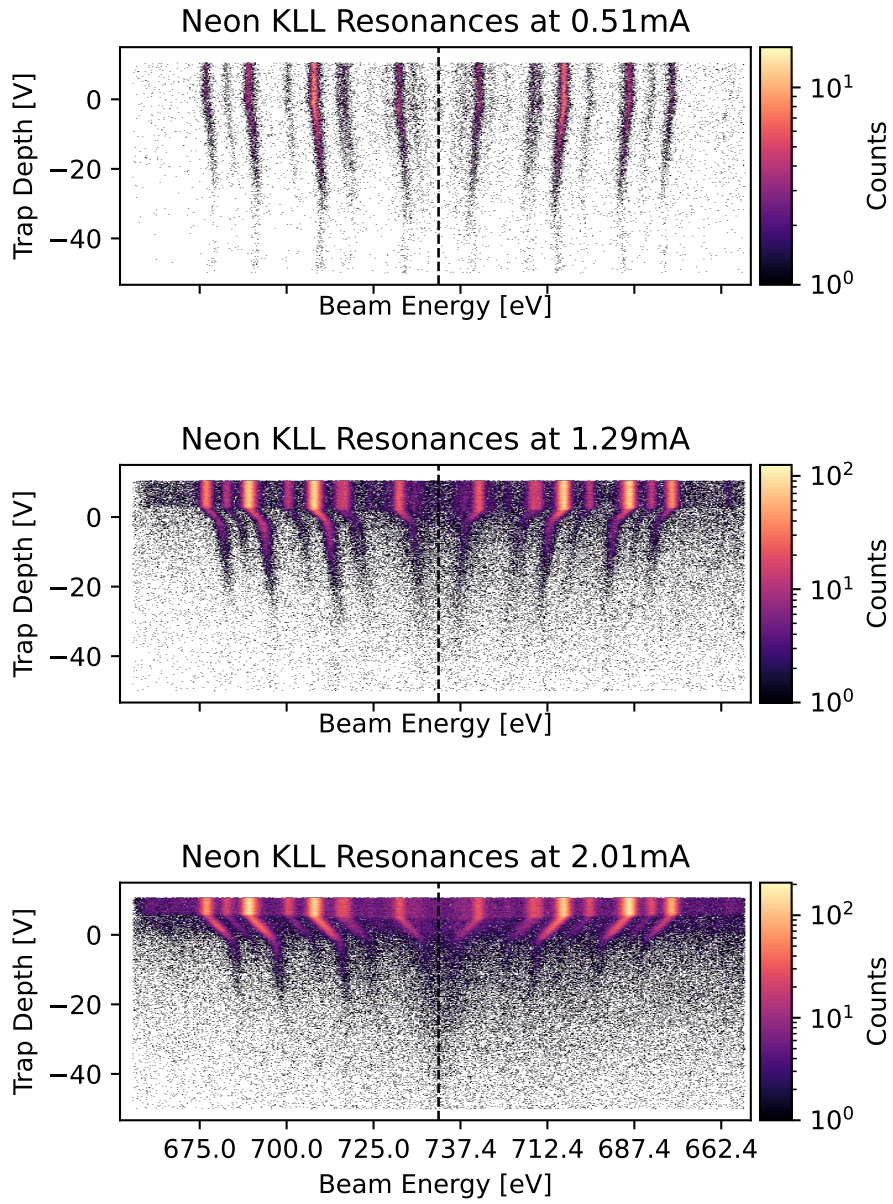
Figure 4.2: Neon KLL resonances at different trap depths and three different currents. The data was acquired continuously as described in 3.5, the current was ramped from 0.5 mA to 2 mA in 20 steps. The current is given with an expected standard deviation of ± 0.02 mA. The given beam energy is not adjusted for space charge effects. Note: The energy axis decreases again after the centre, marked by the dotted line.

4.2 Corretion for Amplifier

The voltages for the drift tubes given in table 4.1 are target values that the actual voltages have been measured independently. The voltage is created by taking the target value dividing it by 400 and generating the ramp described in 3.5 with the divided target values as minima and maxima, the signal is then amplified with a Trek 677B amplifier. The expected gain factor of the amplifiers is 400 but in my measurements, I found a gain factor of 401.26 ± 0.04 together with an offset of 0.03 ± 0.04V for the amplifier used for the outer drift tubes. Deviation from the linear slope never exceeded 0.2V which is also the error of the multimeter used for this measurement. The gain factor for the central drift tube was determined to be 399.36 ± 0.04 with an offset of 0.08 ± 0.05. Here the maximum deviation from the linear fit is 0.1. Due to the very low deviations from the fit and a claimed slew rate of greater than 15 V/µs [16], I assume that during the ramping of the beam energy over 2 seconds and a voltage range of less than 200V, the real gain factor matches the fitted gain factor at all times. These different gain factors mean that the trap depth also changes with the beam energy, as the trap depth is just the difference between the central drift tube used for the acceleration of the beam and the outer drift tubes. This effect is accounted for in fitted lines but not in the histograms shown. It causes a difference of 0.4 V over the whole energy range. An example of this is visible in Figure 4.2, where in the lower two panels the region where the resonancies do not change position over different trap depths seems to begin earlier when the beam energy is higher. The actual resulting voltage minima and maxima are listed in Table 4.2.

4.3 Line attribution

To verify that the lines seen in Figure 4.2 are indeed Neon KLL resonances, I project the counts above a trap depth of 0V up to 10V onto the energy axis. This graph can be compared to theoretical resonance energies shown in figure 4.3. The measured data has to be shifted relative to the nominal beam energy

Table 4.2: Actual Voltages at Drift Tubes

Center Drift Tube Minimal Voltage	404.4 V
Center Drift Tube Maximal Voltage	494.3 V
Minimal Trap Depth at Minimal Beam Energy	-48.3 V
Minimal Trap Depth at Maximal Beam Energy	-47.8 V
Maximal Trap Depth at Minimal Beam Energy	11.9 V
Maximal Trap Depth at Maximal Beam Energy	12.3 V

to compensate for space charge effects. For the shown example at 0.51mA this difference is -7.8 ± 0.9 eV, as determined by taking the mean of the difference in position of the first 7 peaks, the position of which was determined by fitting Gaussians to the data.
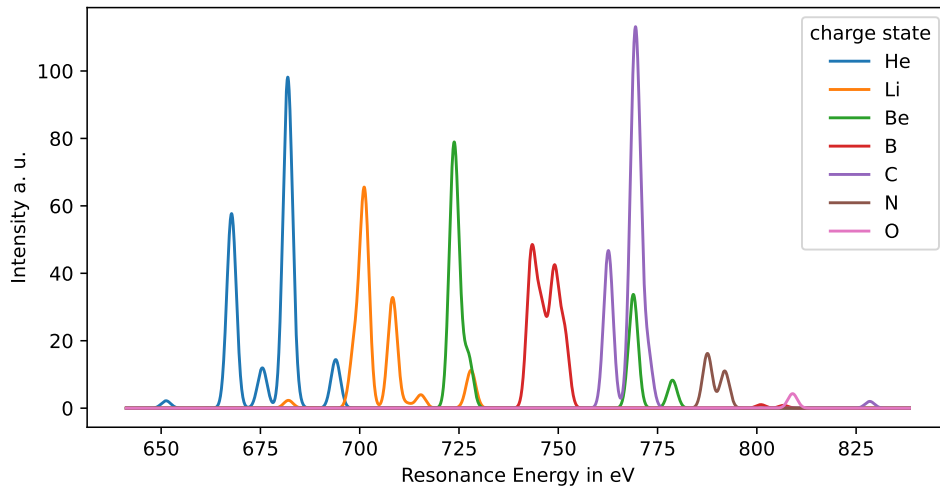

Figure 4.3: Theoretical KLL resonances of the different charge states of Neon and their expected intensities. The data was convoluted with a Gaussian to reflect the expected width in measurements. [7]
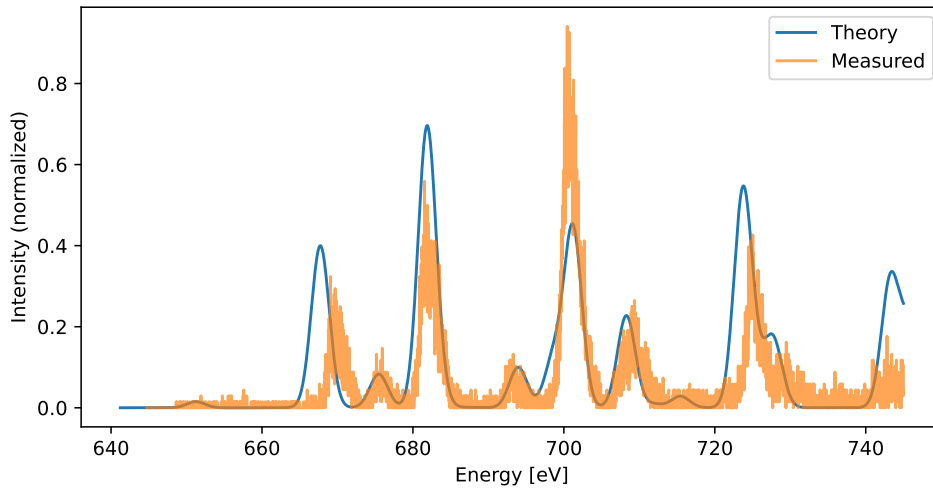
Figure 4.4: The sum of the theoretical resonances from Figure 4.3 overlayed with the counts of photons in a range of 0 to 10 V trapping depth at a current of 0.51mA. The measured data was shifted by -7.8 eV relative to the nominal electron beam energy.

In Figure 4.4 it is apparent that while all the expected peaks are visible, their positions still differ from the theoretical line positions even after accounting for the overall shift due to space-charge effects and losses. This might be partially due to inaccuracies in the theoretical positions as Harman, whose numbers were used for the theoretical lines only claims accuracy within 5-10eV[7].

Another possible explanation is that dielectronic recombination recombines a portion of the ions and therefore reduces the space charge compensation. The effects of changing space charge is investigated further in section 4.6. Notable is that the differences as can be seen if Figure 4.5 do not follow a linear trend which makes a two-point calibration non-viable. Another observation that can be made in Figure 4.5 is that the differences are smaller when the electron beam energy decreases, which would suggest a higher ion content in the trap.
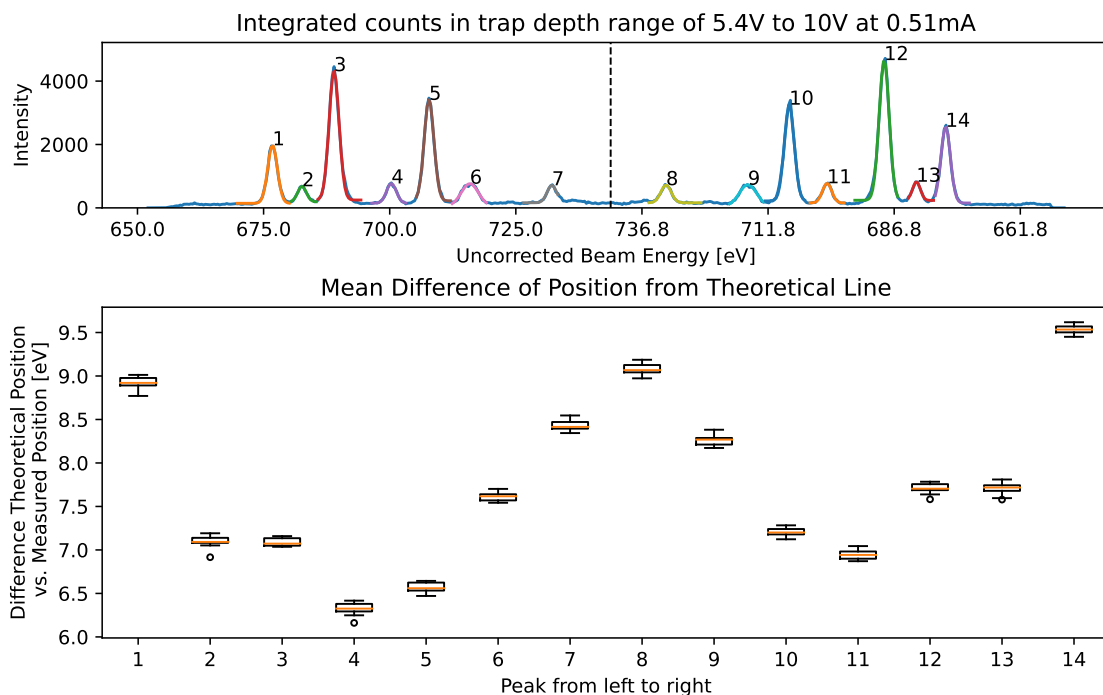
Figure 4.5: The top panel shows an integrated view of the peaks for reference. The bottom panel shows the mean difference between the peak position as determined by a Gaussian fit on the measured data and the model, averaged over all measured electrical currents. The boxes extend from the lower to the upper quartile values, the whiskers extend 1.5 times the height of the box from the bottom or top of the box (The Interquartile-range). Points outside of that range are considered outliers and are drawn as circles.

4.4   Effects on the Effective Beam Energy

When changing the trap depths the measured lines show three distinct sections, highlighted in Figure 4.6, which have different effects determining the observed resonance energy. The first section is located where the trap is closed with trapping potentials in the 0 to 10V range. In this area, the effective resonance energy barely changes, likely because trapped ions and electrons in the beam cancel each others charge. In the second section, the position of the resonancy rapidly moves to higher electron beam energies with falling trap depths, the effect becoming stronger with higher electrical currents. This is caused by the space charge compensation of the ions. With a reducing trap-depth, fewer and fewer ions are trapped and there is less and less compensation for the negative potential of the electron beam. The

last section shows a similar move to higher electron beam energies as for lower trap depths, but the effect is smaller and current independent. By changing the trap depth, the beam energy changes due to the reach-through effect discussed in 2.1.3. This effect is naturally also present in sections 1 and 2, but the effect is isolated in stage 3 as the space charge compensation of the ions is no longer present as ions do not get trapped at these potentials anymore. The count rate in this section is much lower as atoms have to be ionized in rapid succession and then recombine in the short time they spend in the trap before escaping due to their temperature or the pull of the inverted trap. Due to the changing amount of ions in the trap in the different sections, the amount of dielectronic recombination also changes, which leads to the expectation that the intensities also reflect the three outlined sections. This is indeed the case and can be seen in Figure 4.7 although the distinction is a lot less clear in that plot as supposed to the resonance position.
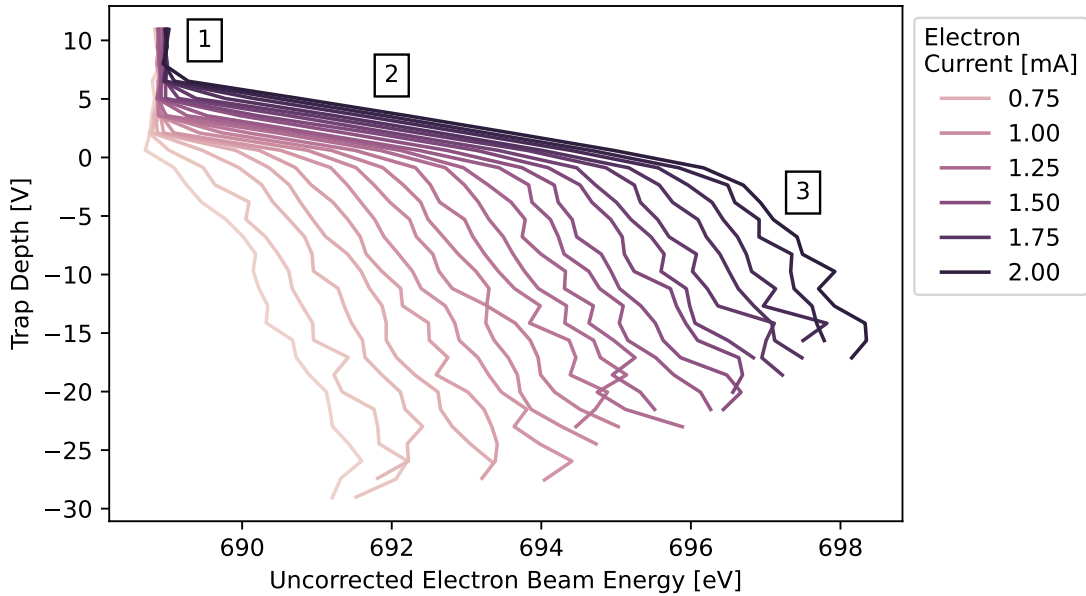
Figure 4.6: Fitted line position of the strongest resonance line of helium like neon (No. 5 in Figure 4.5). The three sections are 1 where the trap is closed and the resonancies do not move, section 2 where fewer and fewer ions are trapped with falling trap depth and finally section 3, where ions are effectively not trapped and electrostatic reach-through dominates the changes in effective beam energy.
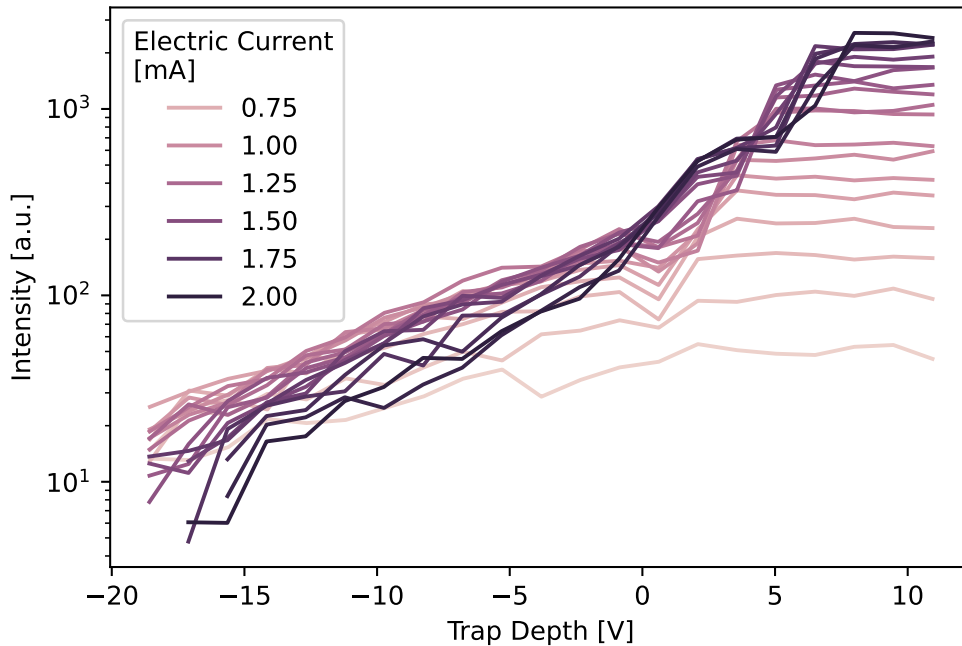
Figure 4.7: Logarithmic intensity of the strongest resonance line of helium like neon (No. 5 in Figure 4.5). A change in the slope of the intensity can be observed at the boundary points of the sections outlined in Figure 4.6

4.5   Electrostatic Reach-Through

To properly estimate the space charge compensation to further investigate the electron beam and ion cloud, the effect of the electrostatic reach-through has to be determined so that it can be subtracted from the space charge effects. This is done by calculating the slope of the lines in section 3 of Figure 4.6. The effect is expected to be linear as it is the result of a simple superposition of the potential of the outer and inner drift tubes with a constant factor c caused by the distance between the drift tubes.

$$V_{\text{DT4 Effective}} = V_{\text{DT4 Target}} + c(V_{\text{DT3}} + V_{\text{DT5}}) \tag{4.1}$$

To determine the slope of the measured resonances, their position at different trap depths had to be determined first. This was done by taking small trap depth slices, integrating over the count rate and then fitting a Gaussian with an offset

26

to them. The fitted offset permits us to remove the background when we look at the intensities of the respective lines later. An example of the result is shown in Figure 4.8.
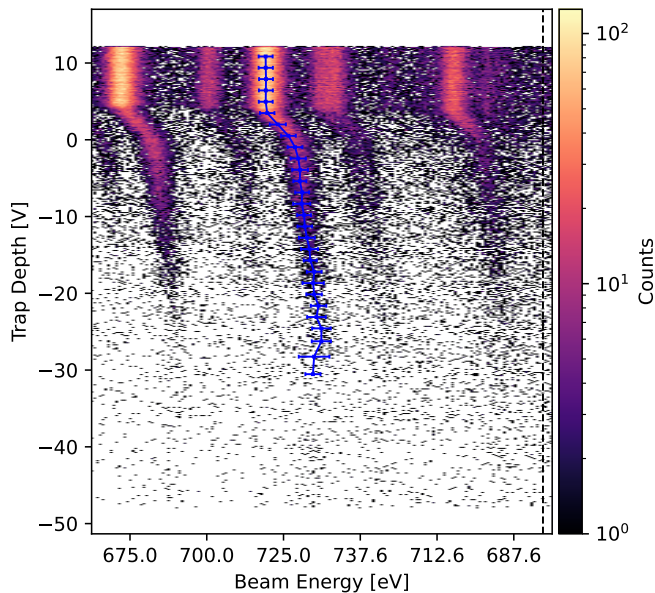

Figure 4.8: A fit tracing the strongest line of lithium like neon ions (No. 5 in Figure 4.5). The error bars are the standard deviations of the individual Gaussian fits.

Next, a line was fitted through the third section of the line for all electric currents, using orthogonal distance regression (see Figure 4.9). Here the error on the energy axis was weighted with the intensity so that the values at very inverted trap settings, where the count rate is low, do not have as high of an impact. The slopes should match within error and reflect the impact of the reach-through onto the effective electron beam energy per trap depth voltage. The different slopes over the electric currents are shown in figure 4.10.
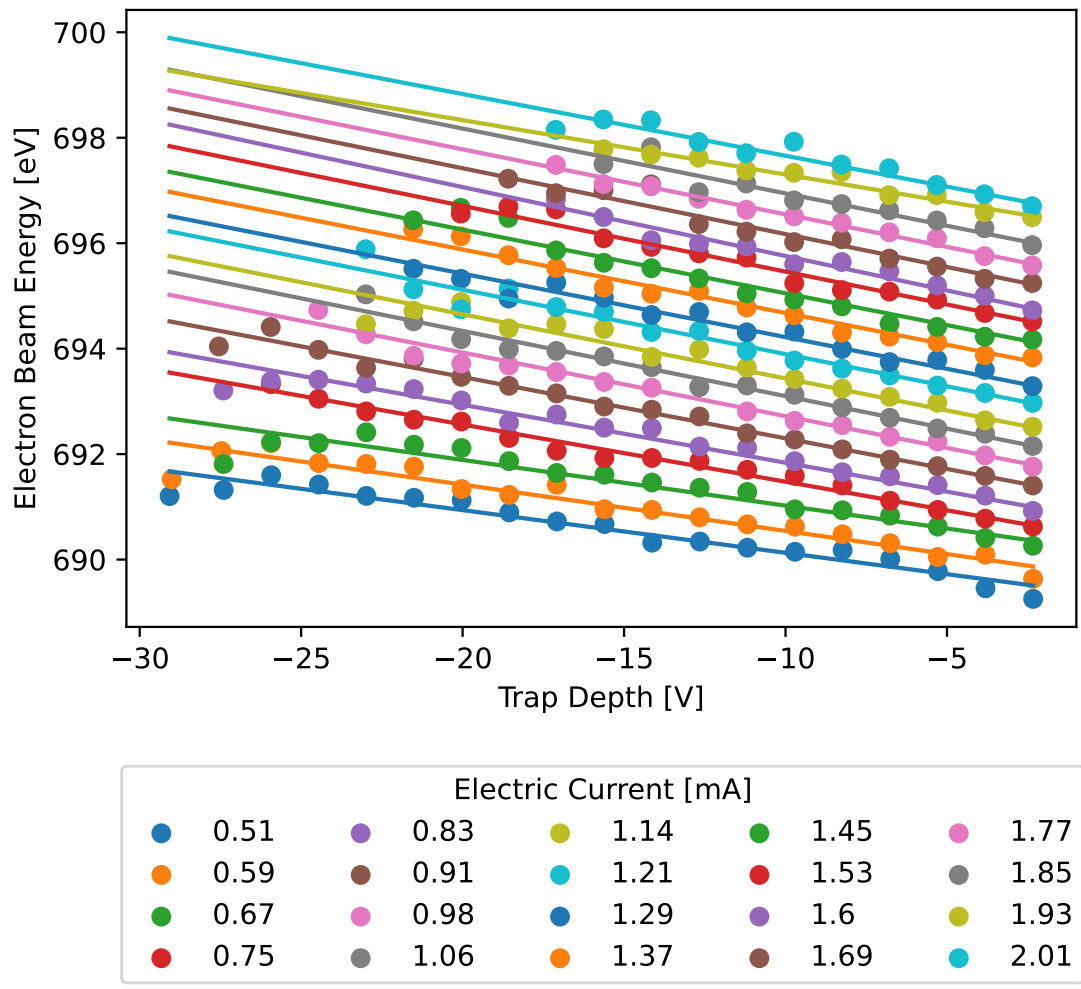
Figure 4.9: A fit tracing line No. 3 (see Figure 4.5) along section 3 (specified in 4.4), at all captured currents. Errorbars where omitted for readability.
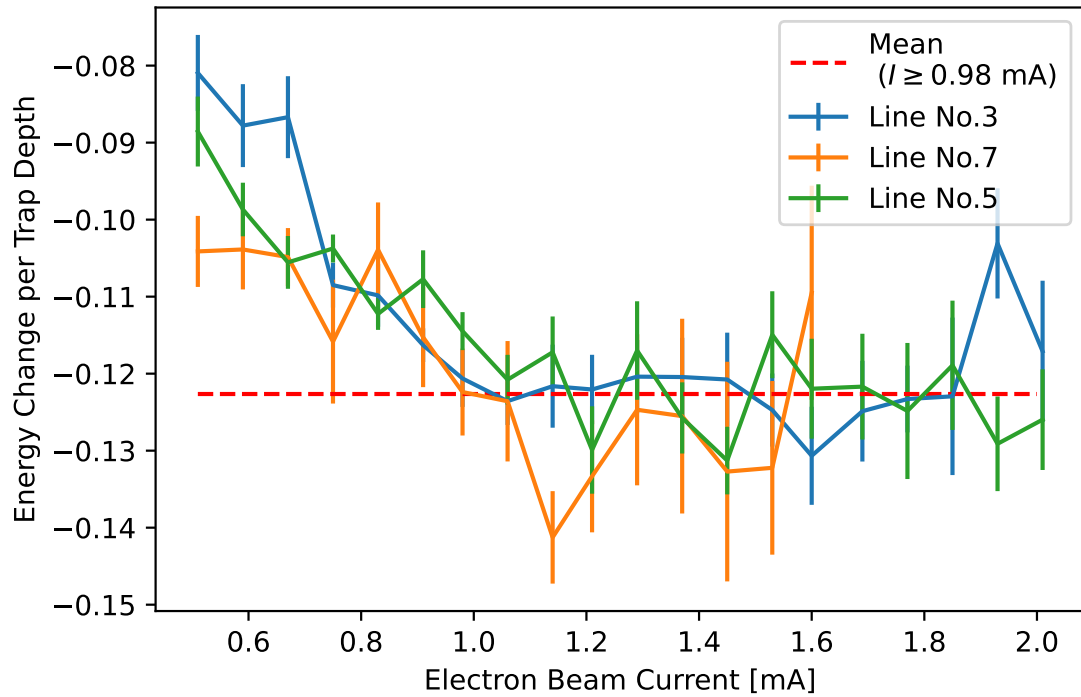
Figure 4.10: The different slopes of the fits in Figure 4.9 with their respective errors. Additionally the same data is shown for line No. 3 and 7.

Using the mean of those slopes it is now possible to remove the effect of electrostatic reach-through from our data. An example of this is shown in Figure 4.11 where the correction was applied to Figure 4.6. The calculated mean is -0.12 ± 0.02 eV/V while only using values measured at and above 0.98 mA. Below that value, the slopes are shallower and afterwards stabilize to the calculated mean. This strongly suggests that there is another current dependant effect at play, which I disregard in this work.
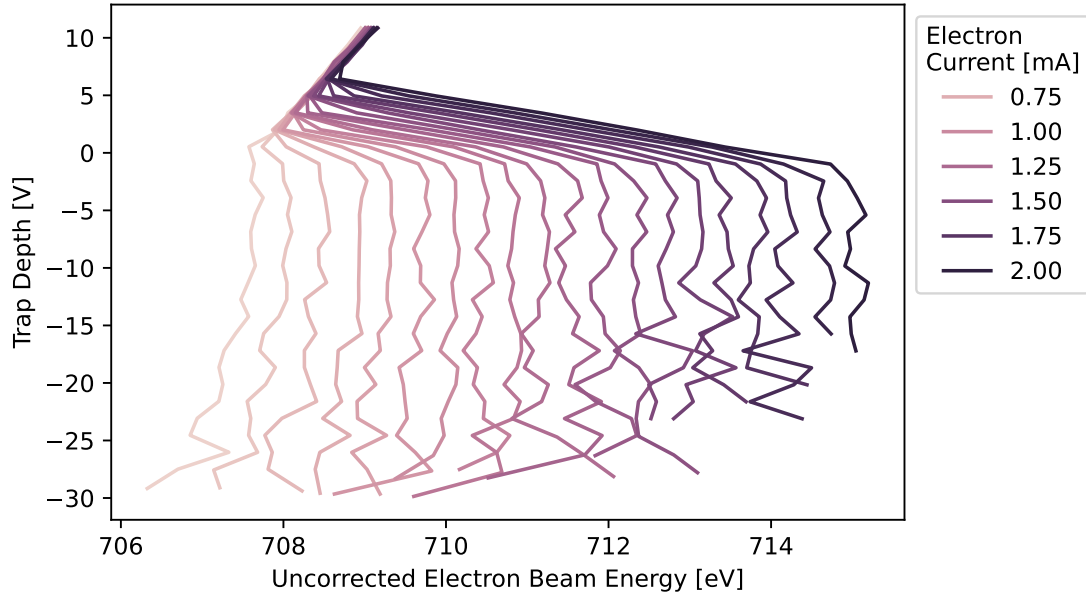
Figure 4.11: Figure 4.6 with corrections for electrostatic reach-through applyed on the energy axis.

4.6   Space charge compensation

To calculate the effect of the space charge compensation, we take a closer look at section 2 marked in Figure 4.6. In this section the trap transitions from a closed configuration with positive trap depth to an inverted state at around -2V. During this transition, ions start to escape the trap axially reducing the space charge compensation and therefore causing the visible shift in the position of the resonances. As can be observed in Figure 4.6 this is a process that is linearly dependent on the current, so that at higher electron beam currents a larger shift is observed. The higher currents have two major effects: For one a higher electron current means more electrons in the beam and therefore a higher negative space charge compensating the acceleration potential between the cathode and the central drift tube, decreasing the energy of individual electrons and as a result moving the resonancies towards higher energies in our measurement. On the other hand, a higher negative space charge also means a higher trapping potential to capture ions. As we have already seen in the bottom panel in Figure 4.5 we do not observe large shifts in peak position when the trap is closed and the current changes, this is most likely the case due to an equilibrium of a kind where the number of ions increases with the current just so that the overall space charge remains constant.

This means that the higher radial trapping potential actually translates to more ions in the trap. By finding the boundary points of section 2, it is possible to calculate the energy shift per current and or the space charge compensation for individual electric current settings.

There are two methods to find the relevant boundary points: Calculating the intersections of linear fits through each section. Or finding the points where the intensity of the resonance changes its trajectory. Both methods should yield the same positions as they both depend on the number of ions in the trap. The intensity plot does show changes in intensity at the points in question but has some additional features that make it difficult to use for fitting purposes, which is why the resonance energy was chosen for the following analysis.

To find the boundary points two additional linear fits were done in addition to the fit of section 3 that was already done in section 2.1.3. The first is done through section 2 and the other one through section 1. The boundary points are then calculated from the intersection of the fits. This can be seen in Figures 4.12 and 4.13. Especially for low currents section 2 only happens over very few data points, which calls the accuracy of the fit into question, but as it will become clear in the following, the slopes calculated using the fits follows the expected linear trend over the different currents, which increases my confidence in the validity of these fits. Taking the boundary point between sections 2 and 3 for each current setting allows us to observe the isolated impact of the space charge of the electrons as we assume that at this point no ions are in the trap to compensate for the space charge of the electrons. By extrapolating the resulting line to an electron beam current we can calculate the 'true' resonance energy where the electron beam energy is not changed by influences of the electron beam or the ions and therefore should match exactly the energy we calculated from the acceleration voltage. The different positions of the boundary point for different currents are shown in Figure 4.14. The extrapolated resonance position is 705.39 ± 0.04 eV which is 4.2 eV higher than the theoretical[7] resonance position and 2.2 ± 0.3 eV lower than the nominal position when the trap is closed which is 707.6 ± 0.3 eV. With this shift we can calculate all the resonance positions based on their position when the trap is closed assuming that the space charge does not change significantly, the result of this is summarized in Table 5.1. The 4.2 eV difference between theory and measurement is most likely due to some loss in voltage that the direct measurement at the amplifier did not capture. A prime suspect here is the heating voltage at the cathode.

By calculating the energy difference between the two boundary points we can calculate the total compensation caused by the ions at any given current. The calculated differences are shown in Figure 4.15. The fit shows that per mA current an additional shift of -4.22 ± 0.03 eV is observed due to the increased count of

31

electrons. This higher space charge is as we can see in for example Figure 4.11 then increasingly compensated by ions that get trapped with higher trap depths so that there is very little difference in the apparent resonance energy for electron beams with different currents.
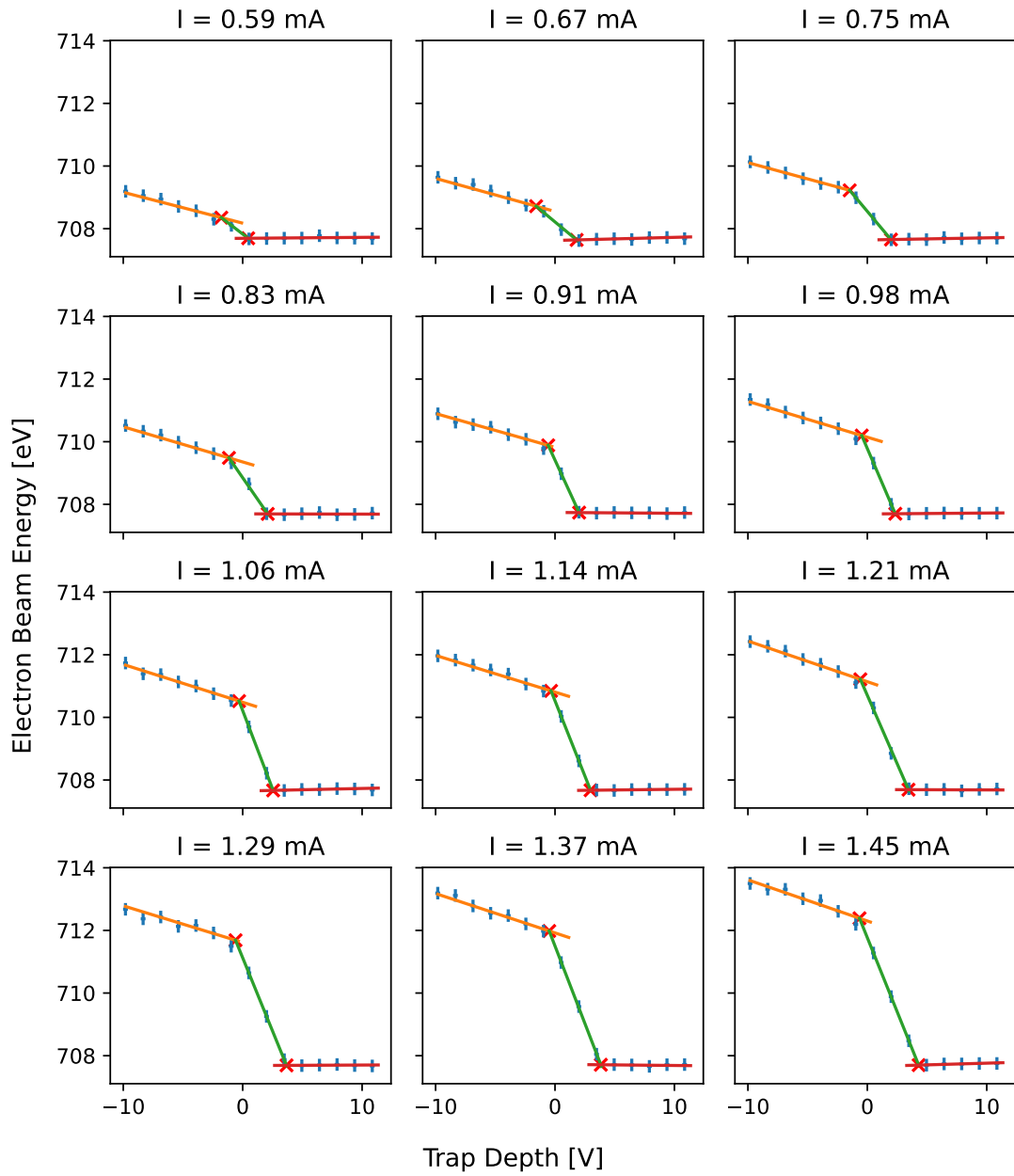
Figure 4.12: Fit of the three sections of line No. 5 with two boundary points as determined by the intersection of three separate fits for each section. The boundary points are marked with a red x, section one is the dark red line, section two is shown in green and section three is orange. Errors shown are the uncertainty of the voltage measurements for the acceleration of the electrons.
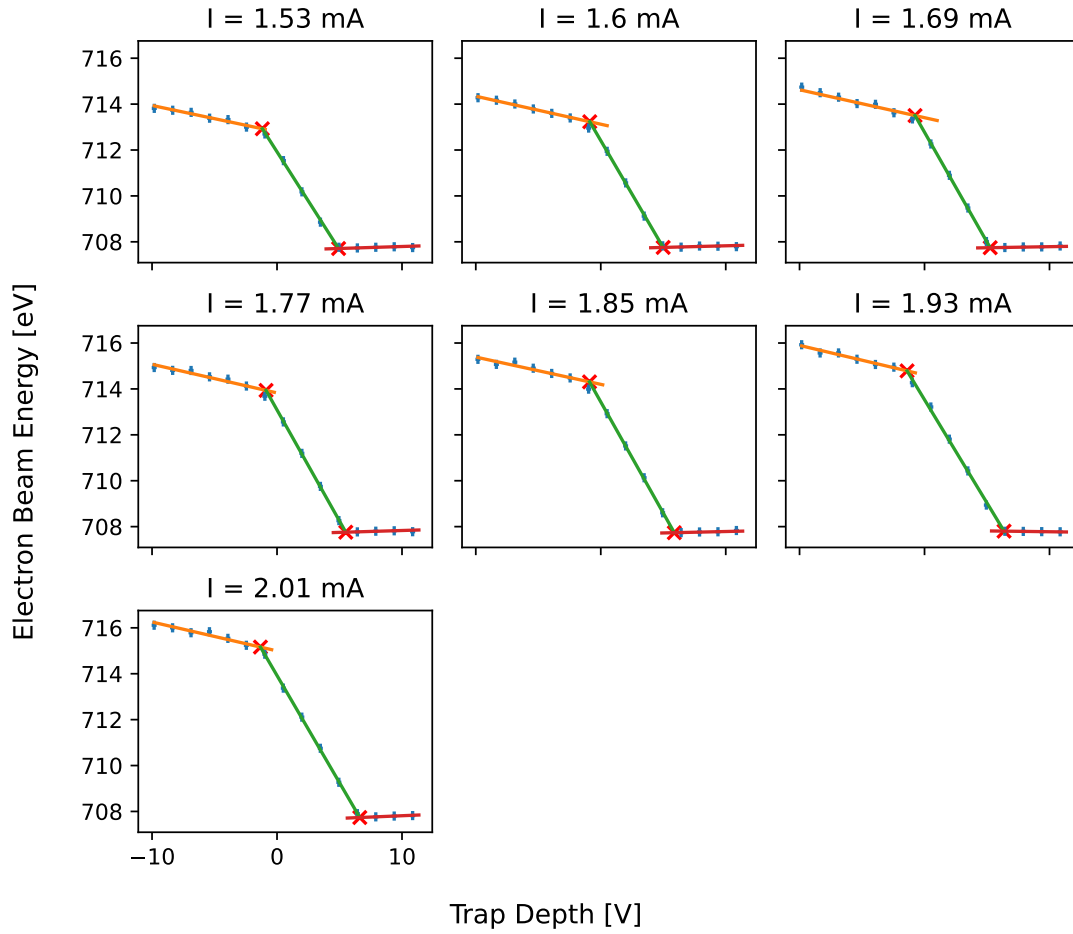
Figure 4.13: Continuation of Figure 4.12 for higher currents.

4.7 Quantifying population of electrons and ions

Knowing the absolute number of electrons in Ions within the trap is not necessary for all applications of an EBIT, for example, spectroscopy of photons emitted in recombination events can be done without little regard for the number of particles interacting. But for other applications like measuring the absolute cross-section of a process, it can be of vital importance. One can estimate the averaged electron beam density for example, by using the measured values for the electron beam and Equation 2.5.

Plugging in the numbers in Table 4.3 yields an electron velocity of $15.2 \times 10^6 \frac{m}{s}$ for 655 eV and $16.2 \times 10^6 \frac{m}{s}$ for 745 eV of electron beam energy. At 0.51 mA

34
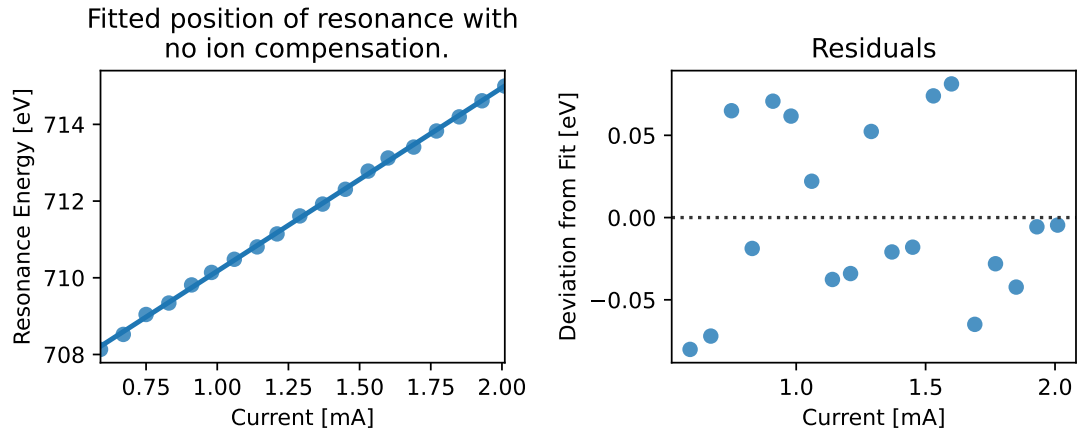
Figure 4.14: The left panel shows the resonance energy of line No. 5 at the boundary point between section 2 and 3 over different currents. Positions are adjusted for reach-through effects. The calculated slope is 4.78 ± 0.03 eV/mA and the intercept is 705.39 ± 0.04 eV. On the right pannel the residuals of the fit are shown.
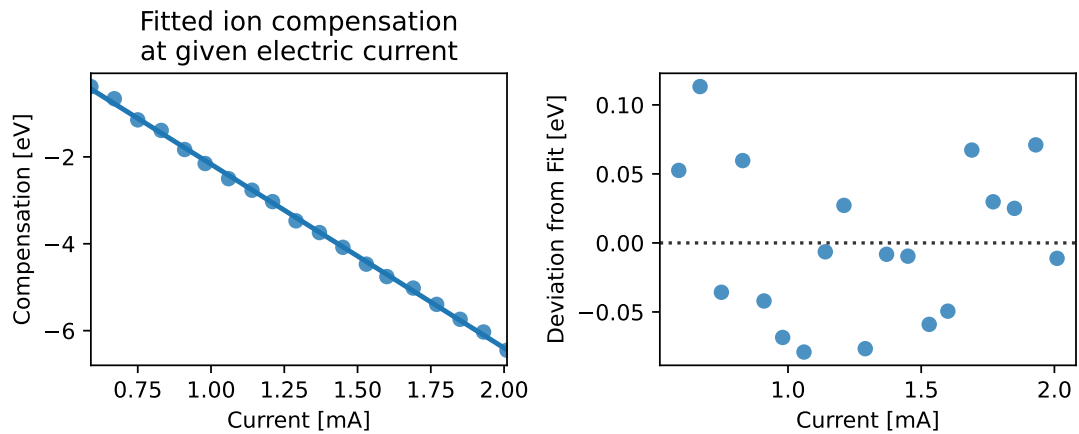

Figure 4.15: The left panel shows the total shift of the resonance energy caused by the ion cloud over the different currents. The calculated slope is -4.22 ± 0.03 eV/mA and the intercept is 2.06 ± 0.04 eV. On the right pannel the residuals of the fit are shown.

this results in an electron beam radius of 68.21 µm and at 2 mA in 68.40 µm. The resulting average electron beam densities are in the range of 1.43×10^{10} to 5.63×10^{10} cm^{-3} for beam currents from 0.5 to 2mA.

Table 4.3: EBIT Dimensions and Parameters [12]

Magnetic Field at Centre of Trap	0.86 T
Cathode Temperature	1400 K
Cathode Radius	1.7 mm
Magnetic Field at Cathode	<100 µT

But these calculations represent only a guess as the herrmann radius is a strongly simplified model. A more realistic value might be obtained by looking at the previously determined space charge inside of the trap. For this pourpose Equation 2.4 can be rearanged to the following:

$$r = exp(\frac{2\pi\epsilon_0 v_e}{I_e}\phi_e(r))r_{dt} \tag{4.2}$$

Here $\phi_e(r)$ is the space charge of the electron beam, which is calculated using the -4.78 ± 0.03 eV/mA determined in 4.6, the actual space charge potential within the beam however is presumably very low due to the presence of the ions.[12] Applying this equation yields an electron beam radius of of 44 ± 1.0 µm at an electron beam energy of 655 eV and 34 ± 0.8 at 745 eV. These radii are about half of what the Herrmann radius suggests. Using this radius we can determine the electron flux in the electron beam. This is simply done by calculating the electron current $\frac{dn_e}{dt}$ from the electric current I using the elementary charge e.

$$\frac{dn_e}{dt} = \frac{I}{e} \tag{4.3}$$

This can then be devided by the area of the electron beam resulting in the electron flux j.

$$j = \frac{\frac{dn_e}{dt}}{\pi r^2} \tag{4.4}$$

Table 4.4: Electron Flux

Current [mA]	Beam Energy [eV]	Electron Flux [$\times 10^{22}\frac{1}{m^2 s}$]
0.51	655	52 ± 3
	745	88 ± 5
2.0	655	203 ± 9
	745	347 ± 20

The number of ions can now be calculated, we have already calculated the number of electrons per second $\frac{dn_e}{dt}$, by dividing that figure by the velocity of the electrons we can get the number of electrons per length. By taking the percentage of compensation α and dividing by the average charge state β and multiplying it by the number of electrons per length we get the number of ions per length.

$$\frac{dn_i}{dl} = \frac{dn_e}{dt}\frac{\alpha}{\beta v_e} \qquad (4.5)$$

In Figures 4.14 and 4.15 the space charge of the electrons per mA was determined to be 4.78 ± 0.03 eV and the compensation per mA to be 4.22 ± 0.03 giving us a compensation percentage of $88.28 \pm 0.07\%$. Unfortunately, I was unable to measure the ion distribution separately so that the true β remains unknown. For now, I will assume the number to be 6.95 which would result from an ion distribution of 35% Helium like, 35% Lithium like 20% Beryllium like and 10% Boron like Ions. The actual values could have been determined by extracting the ions from the trap, a measurement the PolarX-EBIT can be equipped to do which I was unfortunately unable to do due to time constraints. The resulting numbers were multiplied by the trap length and displayed in Table 4.5. The number of a specific population can then be simply calculated by taking multiplying by the ratio, determined by an extraction measurement or in this case the guessed value.

Table 4.5: Number of Ions in the Trap

Current [mA]	Beam Energy [eV]	Ion count times β [$\times 10^6$]	Ion count with $\beta = 6.95$ [$\times 10^3$]
0.51	655	4.63 ± 0.18	670 ± 30
	745	4.34 ± 0.17	630 ± 20
2.0	655	18.26 ± 0.18	260 ± 30
	745	17.12 ± 0.17	250 ± 20

4.8 DR Event Rate

The measured count rates for the resonances can be extrapolated to the actual rate of recombination by accounting for the solid angle of the detector. This corrects for the fact that most photons generated by recombination do not hit the detector as they are emitted in the wrong direction. By multiplying the measured count rate by the ratio of the full solid angle of 4π sr and the solid angle of the detector the total count rate can be calculated. The solid angle can be calculated with the following equation:

$$\Omega = \frac{A_{\text{Detector}}}{r^2} \qquad (4.6)$$

37

The area A of the used detector is 150 mm^2 and together with the distance to the trap centre of $r = 27.7 \pm 0.8$ mm the solid angle is $\Omega = 0.195 \pm 0.011$ sr. This however would be an oversimplification as not all recombination happens exactly at the trap centre. Recombination can happen all along the electron beam and the solid angle should reflect that. The average solid angle can be calculated by using the length of the opening in the trap electrode $l = 15$ mm.

$$\Omega = \frac{1}{l} \int_{-l/2}^{l/2} \frac{A}{r^2 + x^2} dx \tag{4.7}$$

Resulting in a slightly lower average solid angle of 0.191 ± 0.011 sr. This ignores the width of the electron beam, which is small compared to the uncertainty of the detector position and therefore negligible.

Two other effects have to be considered. One is the detector efficiency. Not all photons that fly in the direction of the detector actually result in a measured event. Meshes, windows and the detector material itself might absorb the photon. I will ignore this factor η as the impact is expected to be low, but this means that the actual recombination rates are higher than the numbers given here. The other effect is the polarization, due to which the emission rate of photons is dependant on the relative angle to the direction of the electron beam. This effect is also not accounted for in my calculations. A correction could be made using Equation 2.15 and polarization values from a numerical simulation, made with for example FAC[5].

The actual intensity is therefore given by

$$I_{\text{tot}} = I_{\text{measured}} \frac{4\pi}{\Omega\eta} \frac{3 - P}{3} \tag{4.8}$$

The measured Intensity was determined by taking a slice of each of the captured histograms from a trapping voltage of 6 to 10V and projecting the count rate onto the energy axis and then fitting Gaussians to the resulting plot. The area below the fit within the 3σ range was taken as the count rate and then divided by the time spent scanning the just used area of the histogram. This means the total time spent, minus the time not scanning that specific trap depth range and minus the time not scanning the aforementioned 3σ area of electron beam energy and dividing all that by 20 due to the 20 different current settings. The total time spent capturing the data was over 4 days, the exact timings are listed in Table 4.1. The resulting event rage is shown in Figure 4.16 for line No. 5. Additionally, the count rate was divided by the factor 0.53 ± 0.02 which arises from the unfortunate fact that the MPA system, that records the photon events, not always saves all information for one event, so that sometimes information about the trap depth or beam energy is missing, these photon events can therefore not be displayed in the

histograms. The 0.53 is the ratio of the number of events added to the histogram to the total number of recorded photons. When and why this happens is not clear and warrants further investigation.
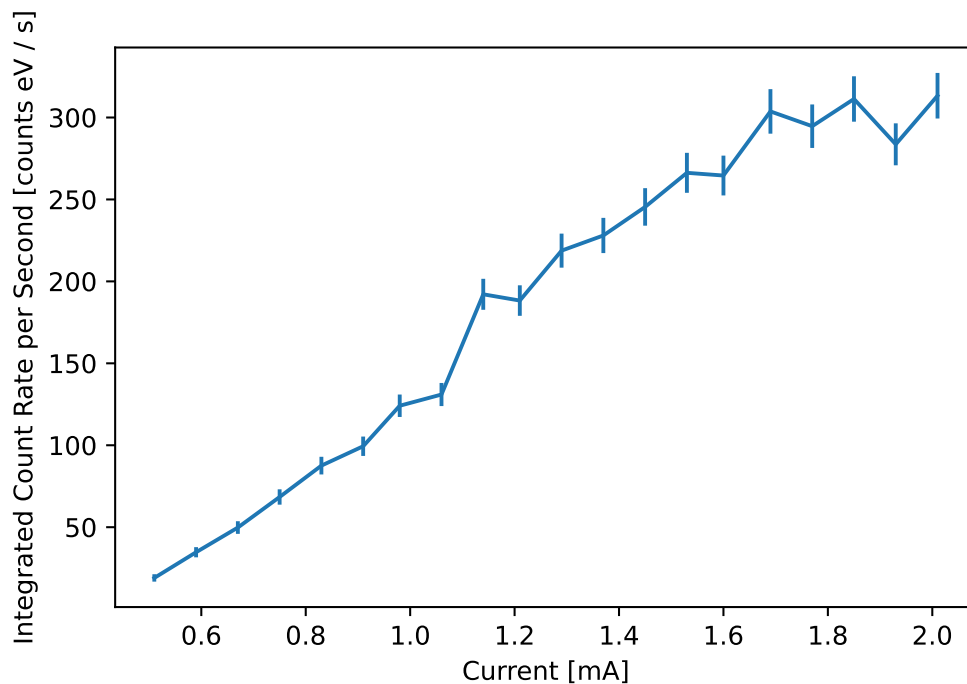

Figure 4.16: Integrated count rate per second of line No. 5. Note that this is the measured count rate and still needs to be adjusted for the solid angle.

4.9 Resonance Strength

The resonance Strength is, as explained in 2.3.2, the integral of the cross-section over the energy. It can be calculated by taking the integrated photon count rate I for a resonance we just calculated in 4.8 and multiplying it with the also already calculated electron flux j and the number of ions present N.

$$S = \frac{I}{Nj} \tag{4.9}$$

We can not use the number of ions calculated in 4.7 directly as we only see the photons from resonancies along the 15mm long opening of the trap and the numbers there are given for the full length of 25mm. Therefore the number has

to be multiplied by the ratio 3/5 first. The results of the calculation are listed in Table 4.6, the error was calculated via Gaussian error propagation, but the standard deviation over all different current settings suggests that I underestimate the error of the values.

Table 4.6: Resonance Strength

Line No.	Strength Measured [barn eV]	Standard Deviation [barn eV]	Strength Theory [barn eV][7]
1	101 ± 20	26	87000
2	28 ± 8	7	17980
3	210 ± 40	60	146100
4	31 ± 9	9	26623
5	199 ± 40	50	96100
6	39 ± 9	11	49400
7	69 ± 21	30	112000

The resulting resonance strengths are significantly lower than any of the theoretical values. This discrepancy can not be explained by my ignoring the efficiency of the detector or the polarization. This can have a multitude of reasons. One could be the spatial distribution of the ions and electrons, the formulas here assume perfectly uniform distribution within the calculated radius, this is certainly not the case. Another issue could be the assumed charge state distribution, which could not only be wrong but also omit the contribution of contaminants i.e. other ions like oxygen. Non the less all these factors should not result in a discrepancy as large as seen here.

The possibility has been raised that the theoretical strengths in [7] are not in fact the strength of the dielectronic recombination, but the strength of dielectronic capture. This would mean that the branching ratio between the radiative decay and the autoionization of the excited state has to be accounted for when comparing my numbers with the theoretical ones. Using FAC[5] the branching ratios for the first 6 lines were determined and are listed in Table 4.7

Table 4.7: Branching Ratio Radiative Decay / Auger

Line No.	Branching Ratio	Extrapolated Resonance Strength [barn eV]	Strength Theory [barn eV]
1	1.497	170 ± 40	87000
2	0.076	400 ± 110	17980
3	0.031	7000 ± 2000	146100
4	0.260	150 ± 44	26623
5	0.137	1700 ± 410	96100
6	0.472	122 ± 34	49400

Extrapolating the resonance strength of dielectronic capture from my measurements using those branching ratios still yields significantly lower numbers than expected. Considering the magnitude of the difference, a physical explanation seems

unlikely and a mathematical error can, despite repeated checking, not be ruled out.

Chapter 5

Conclusions and Outlook

This Thesis primary investigated space charge effects due to the electron beam and ion concentration within an EBIT. The measurement of the space charge in combination with basic physical concepts allowed for the determination of the electron beam radius and an approximation of the resonance strength of dielectronic recombination in Neon without reliance on theoretical values.

To facilitate the measurement of the space charge, the resonance energies of KLL Neon dielectronic recombination were measured. The error here is composed of the fundamental resolution of the measurement due to the not perfectly mono-energetic electron beam and the accuracy of the beam energy measurement, the spread of the electron beam energy means that lines within a range of approximately 2 eV can not be resolved separately. Nonetheless, positions of the resulting peeks was consistant within $0.3eV$ or better in the various fits made throught this work. To get the positions of the resonances the effects of electrostatic reach-through the different gain factors of the used amplifiers and the space charge effects had to be accounted for. The reach-through has been found to be -0.12 ± 0.02 eV/V, and the additional space charge per mA was determined to be -4.22 ± 0.03 eV. These errors illustrating the high consistancy of the peak possitions. A summary of the measured line positions along with the theoretical and the positions found in previous works can be found in Table 5.1. The measured line positions differ significantly from the theory and previously measured values. The mean difference to the previously measured values is -5.23eV with a standard deviation of 0.7. This means, as already mentioned in 4.6, there is presumably a constant offset of that size, that I overlooked. If we assume that this is the case, then the positions only vary within 1eV from the previously measured values which is to be expected, as some of the lines measured are multiple transitions overlaying each other, which just could not be resolved separately.

---

[1] E_{lit} was taken from [10] for Helium like lines (1-4) and [9] for Lithium like lines (5-6)

Table 5.1: Line Positions [1]

Line No.	Configuration	Term	$E_{\text{this work}}$ (eV)	E_{Harman} (eV)	E_{lit} (eV)
1	$1s(2s2p\,{}^3P^\circ)$	${}^2P^\circ$	674.5 ± 0.3	667.79	668.75 ± 0.11
2	$1s2p^2$	${}^4P$	680.4 ± 0.3	675.48	674.05 ± 0.13
2	$1s(2s2p\,{}^1P^\circ)$	${}^2P^\circ$		675.49	674.65 ± 0.14
3	$1s2p^2$	${}^2D$	686.7 ± 0.3	681.84	681.16 ± 0.1
4	$1s2p^2$	${}^2S$	698.1 ± 0.3	693.95	693 ± 1
5	$1s({}^2S)2s2p^2({}^2D)$	${}^3P$	705.5 ± 0.3	701.16	700.0 ± 0.4
5	$1s2p^3$	${}^3D^\circ$		701.24	702.0 ± 1.6
6	$1s2p^3$	${}^1D_2^\circ$	713.7 ± 0.3	708.27	709.34 ± 0.11
7			729.9 ± 0.3	723.68	

After this, the measured space charge was used to calculate the radius of the electron beam. The resulting beam radius is 44 ± 1.0 µm at an electron beam energy of 655 eV, its accuracy is limited by the accuracy of the measured space charge. The radius then enabled me to give an estimate of the number of particles inside of the electron beam required to cause the observed total space charge. Assuming all the particles have the charge of $|e|$ the total number of particles is on the order of 10^6. The accuracy of this figure was hampered by the imprecise measurement of current. I then made the assumption, that the average charge of the contained particles is $6.95|e|$ which results in $(260 \pm 30) \times 10^3$ ions trapped if the electron beam current is 2mA and de beam energy is 655 eV. These numbers along with the integrated count rate is enough information to calculate the resonance strength of the individual lines. Unfortunately, the resulting resonance strengths are multiple orders of magnitude smaller than the ones provided by the referenced theoretical calculations, despite rigorous checking I can not rule out a simple mathematical error because, even considering significant uncertainties in the used values, a difference of this magnitude seems unlikely.

The resonance strengths determined here would have been only useful for showing that this is a viable method for measuring the resonance strength of dielectronic recombination. For quantitative measurements, the ion distribution has to be known and a more detailed analysis of the detector efficiency should be done. Lastly, Polarization can have a significant effect and can not be discarded if quantitative results are required.

Future work in this area might want to investigate the presumably temperature-related effects that lead to the seemingly current independent position of the resonances when the trap is closed. Another obvious extension of this work would be a measurement that includes information about the charge-state distribution of trapped ions gathered by an extraction measurement, along with an investigation into the spatial distribution of the electrons and ions inside the beam, as in this

work a homogeneous distribution was assumed to simplify the problem.

# Acknowledgements

Appendix A

Recorded Histograms

This Appendix includes all the 2d-histograms that were used in the analysis in Chapter 4. The Axis were labelled in accordance with the measured electron beam energy and trap depth. The changes in trap depth due to the different gain factors of the amplifiers was not corrected, nor are where there any adjustments for electrostatic reach-through or space charge effects. The dotted line in the histograms indicates the point from which onwards the energy decreases again.
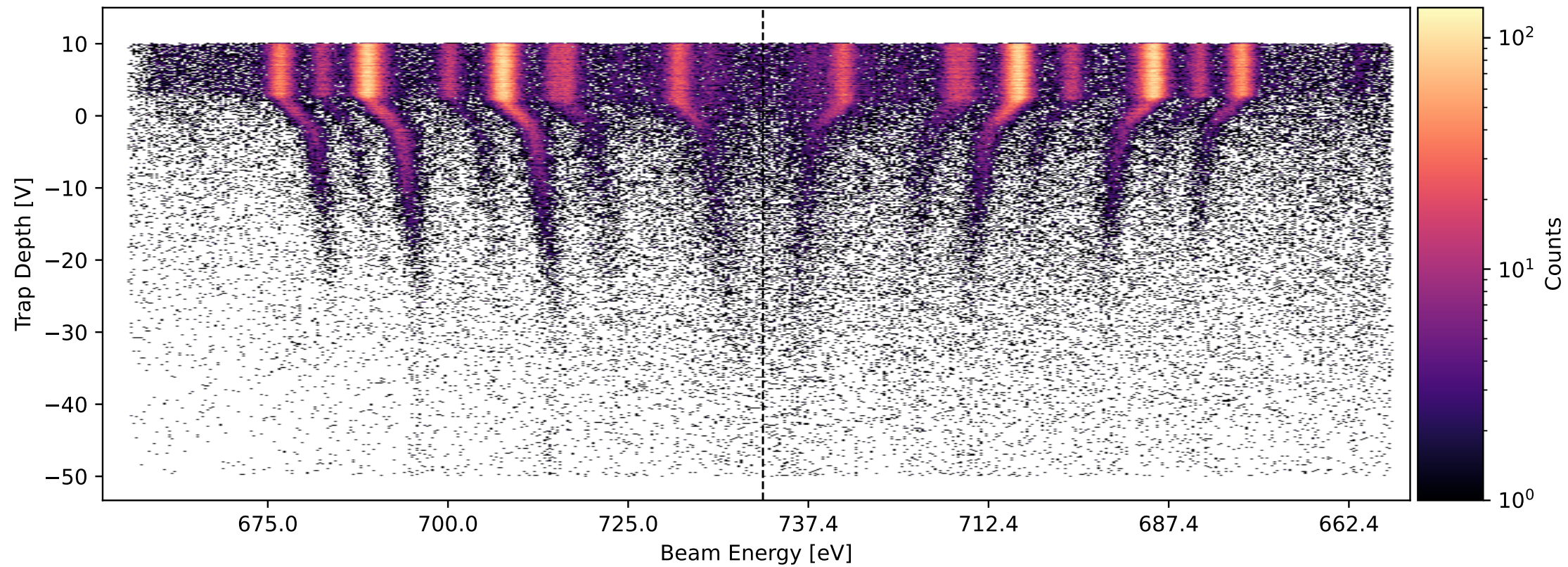
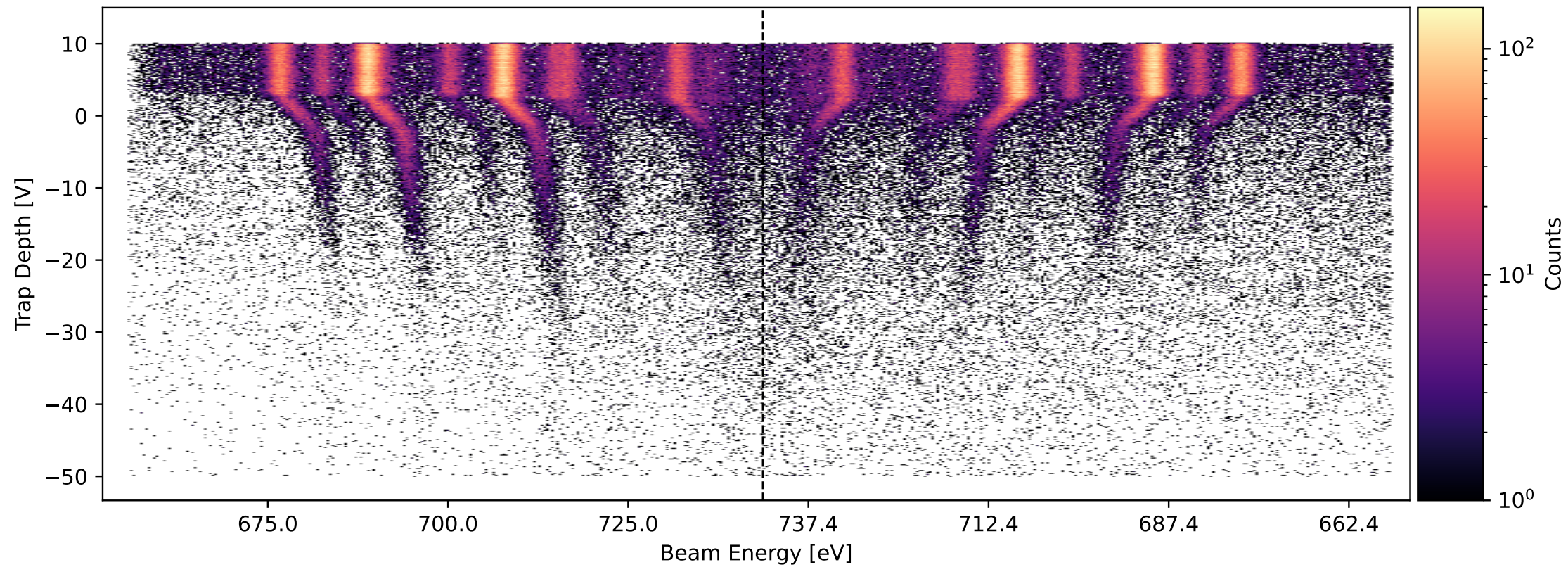Neon KLL Resonances at an Electron Beam Current of 0.51 mA
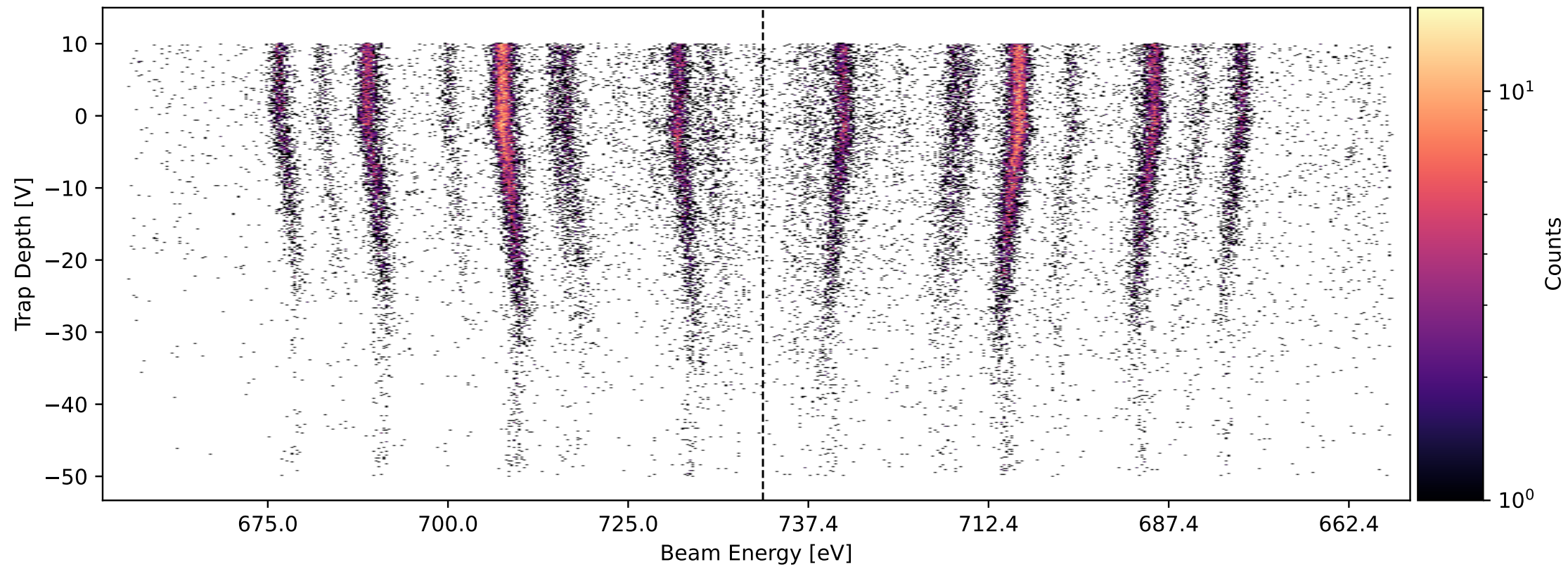
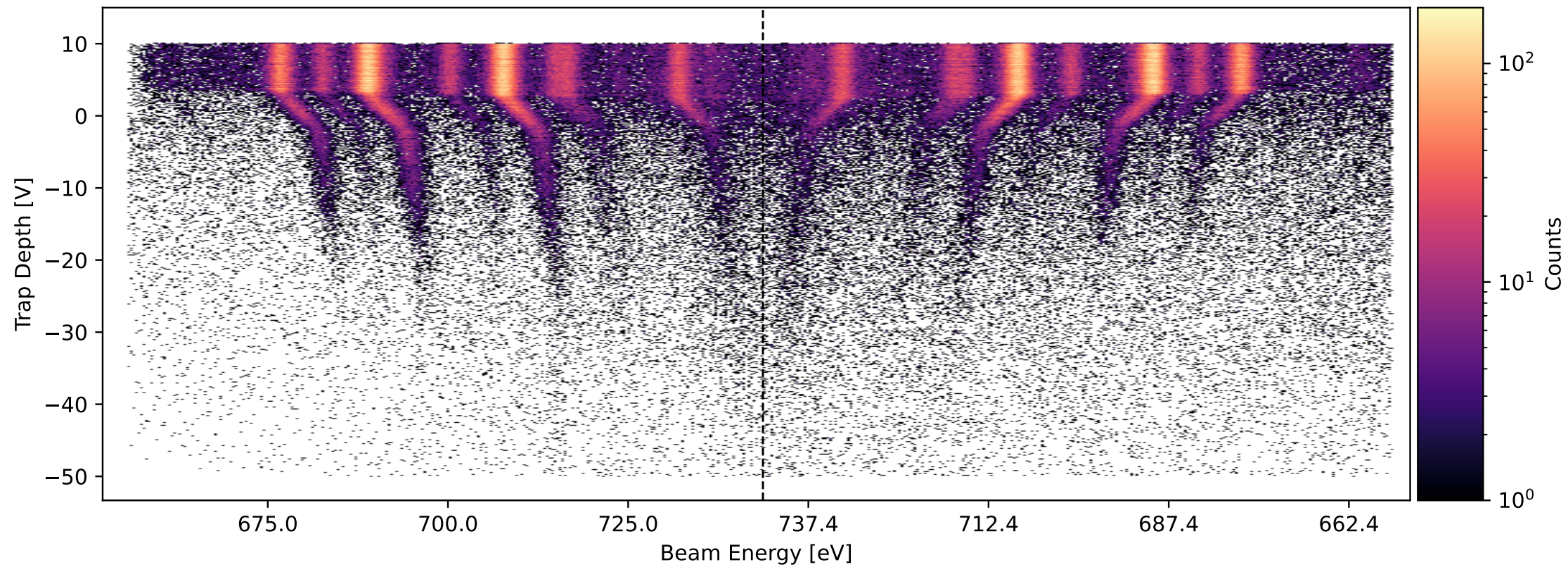Neon KLL Resonances at an Electron Beam Current of 0.59 mA
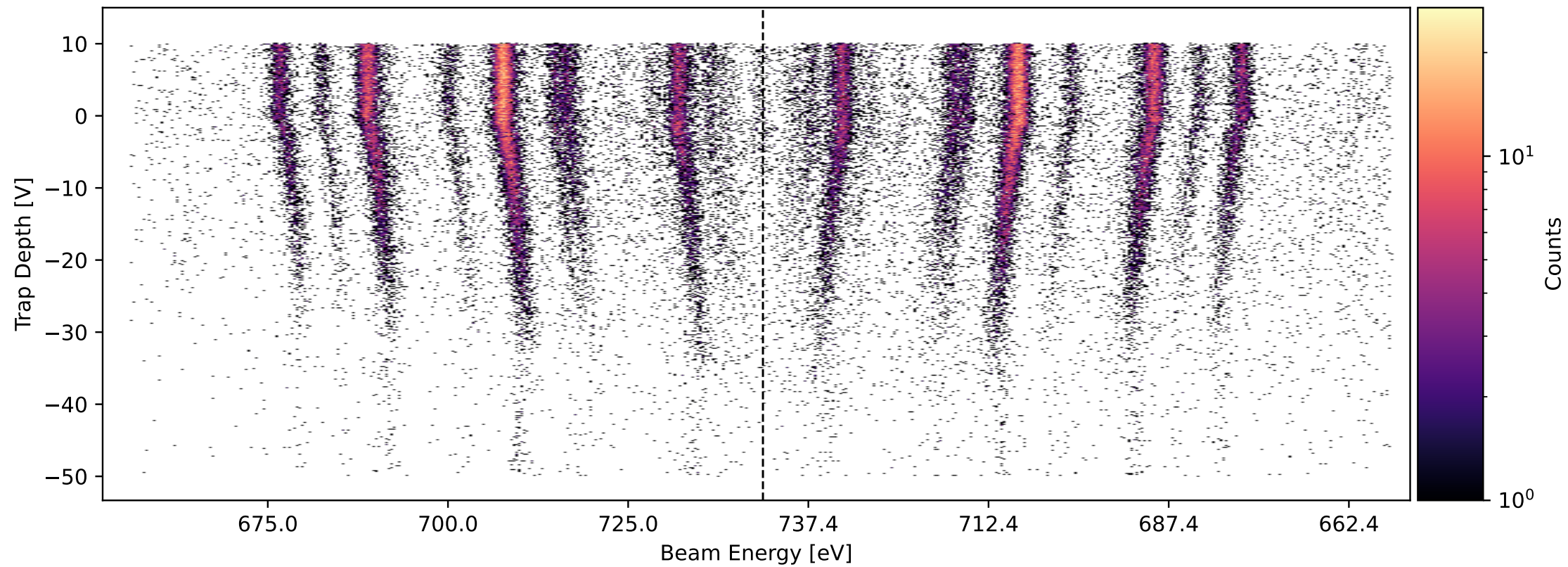
Neon KLL Resonances at an Electron Beam Current of 0.67 mA
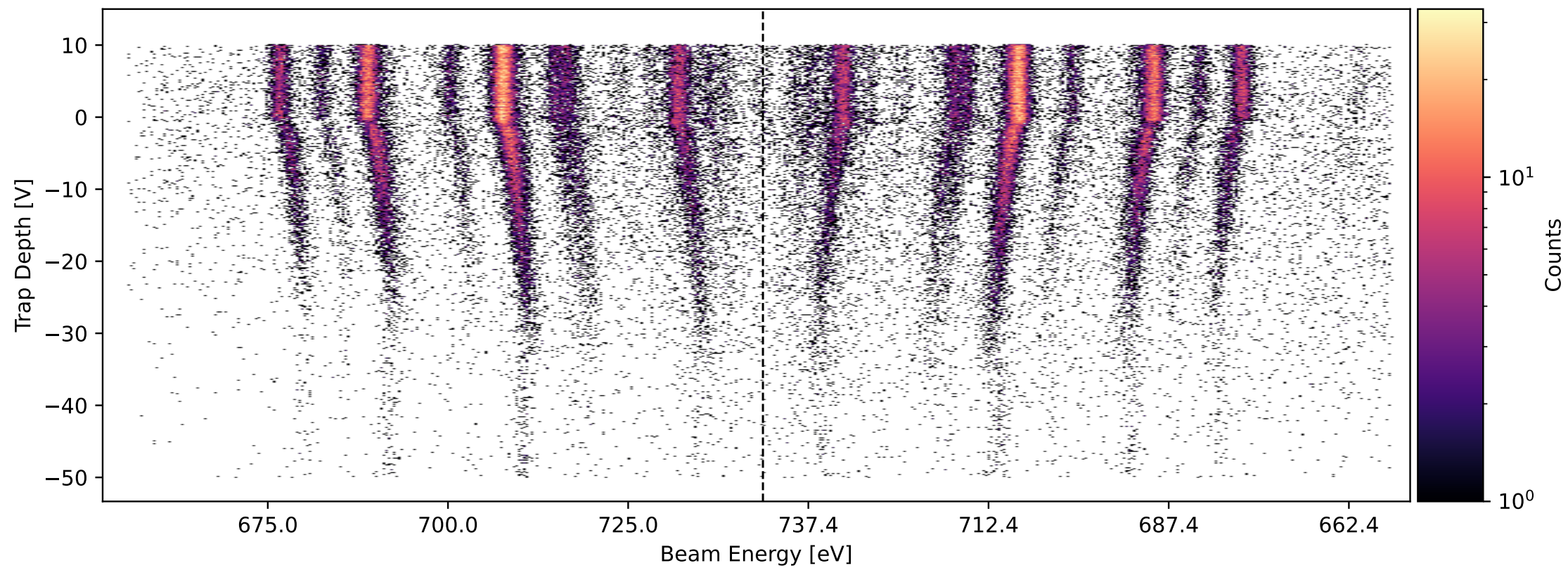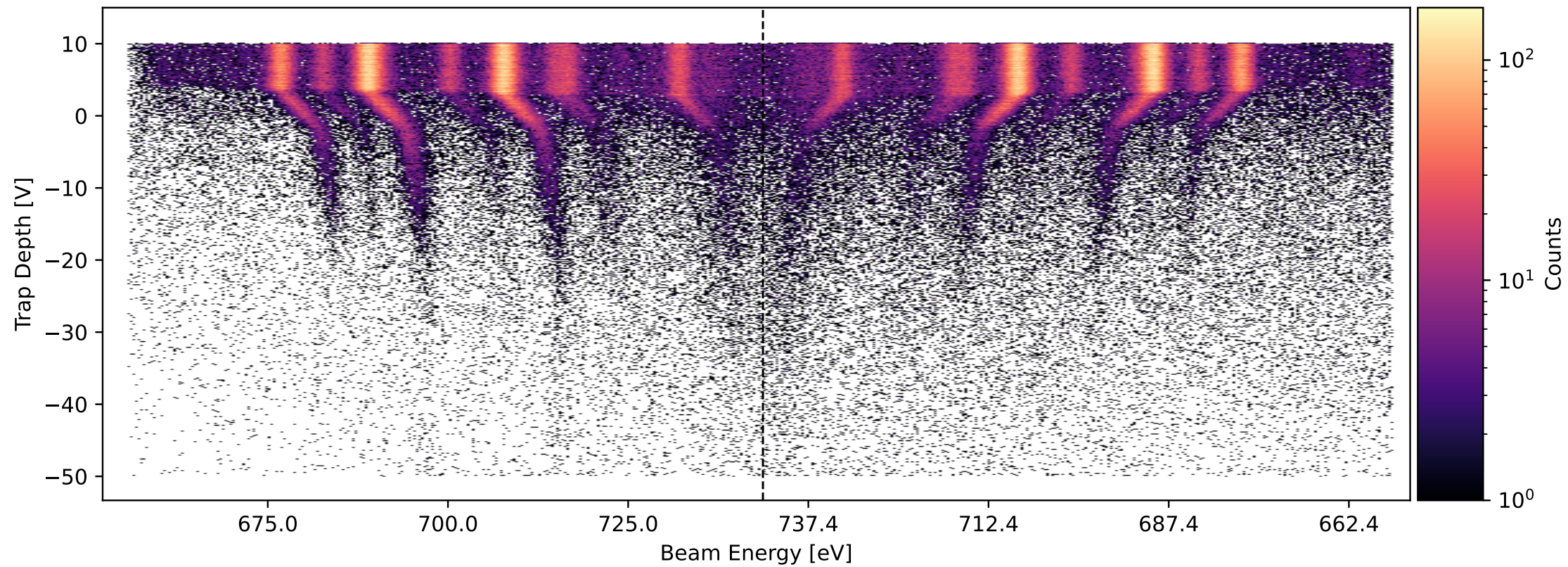
Neon KLL Resonances at an Electron Beam Current of 0.75 mA
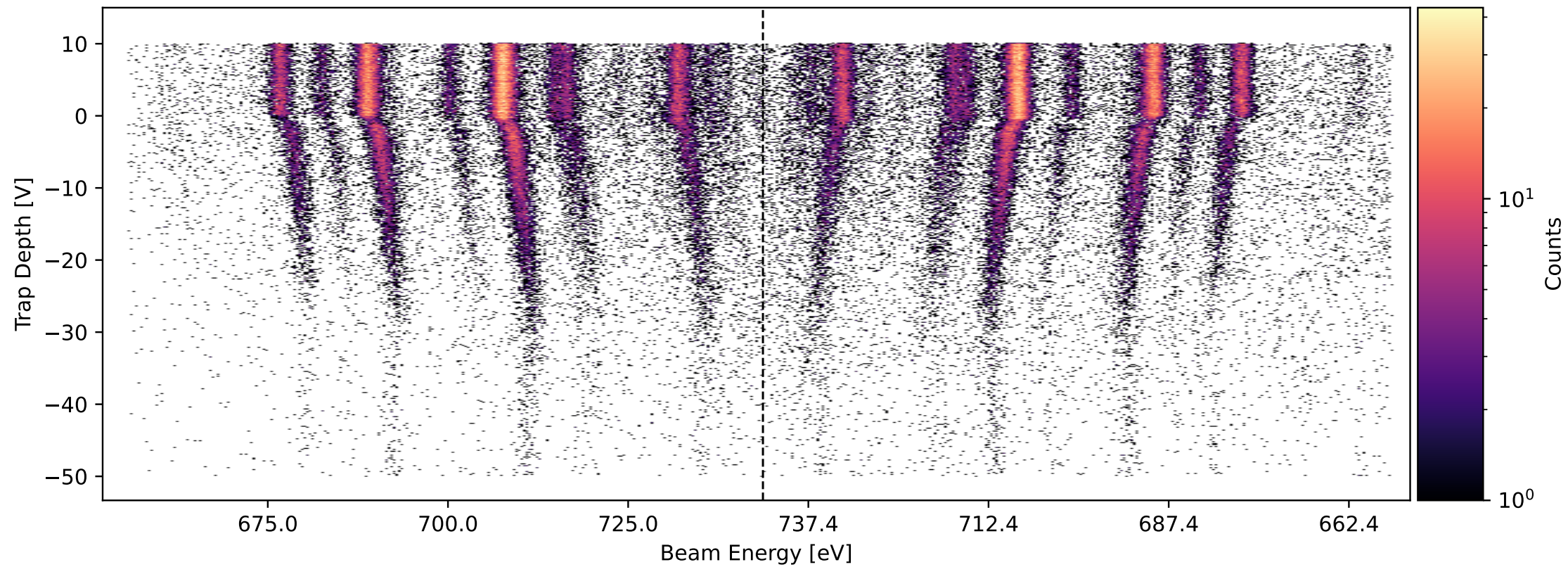
Neon KLL Resonances at an Electron Beam Current of 0.83 mA
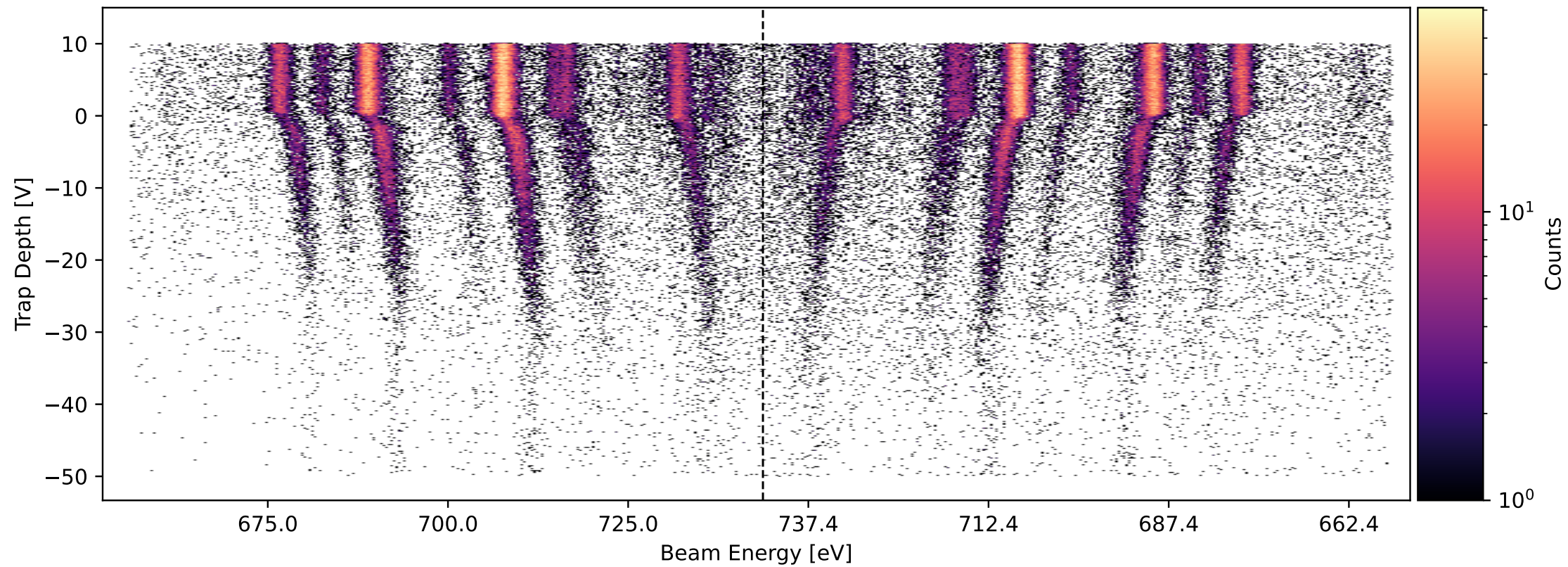
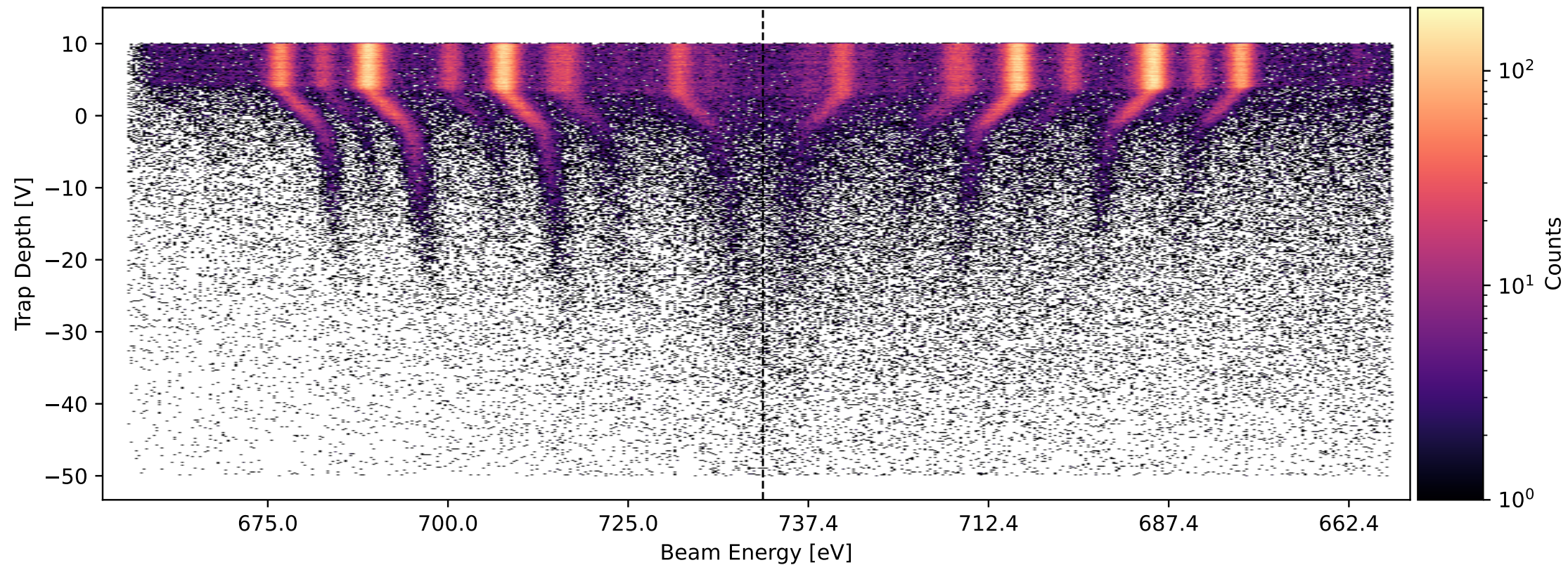Neon KLL Resonances at an Electron Beam Current of 0.91 mA
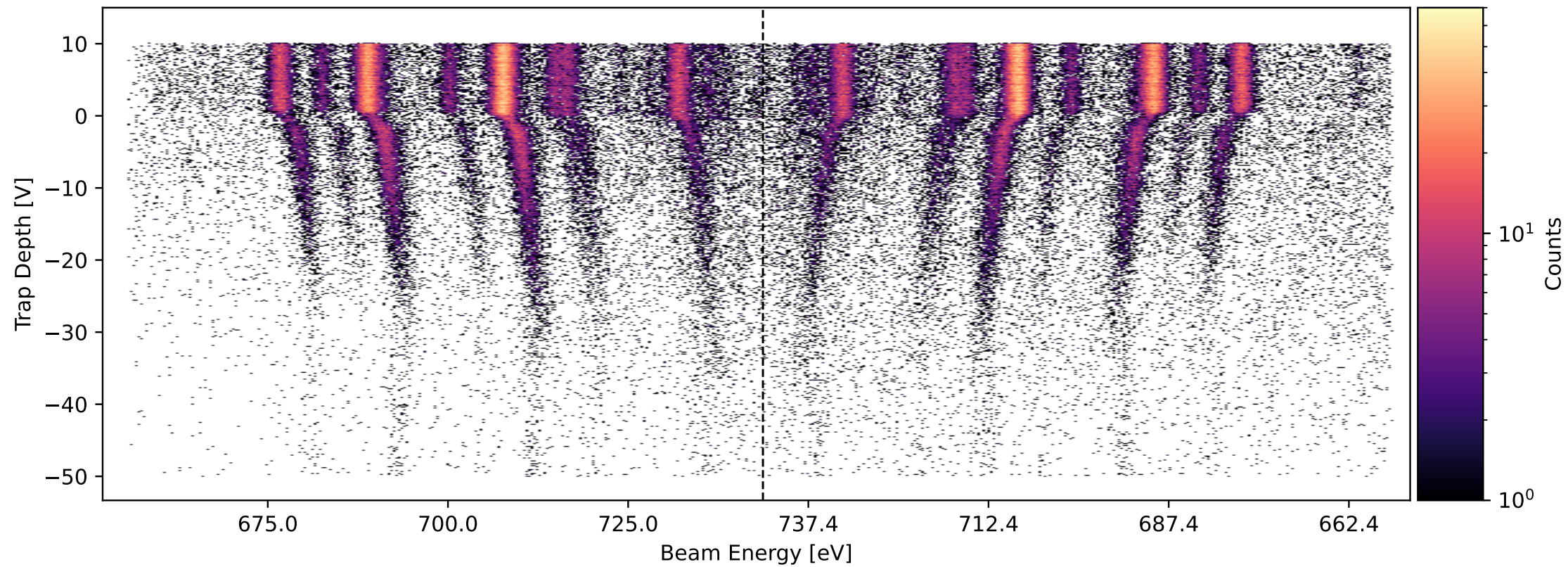
Neon KLL Resonances at an Electron Beam Current of 0.98 mA
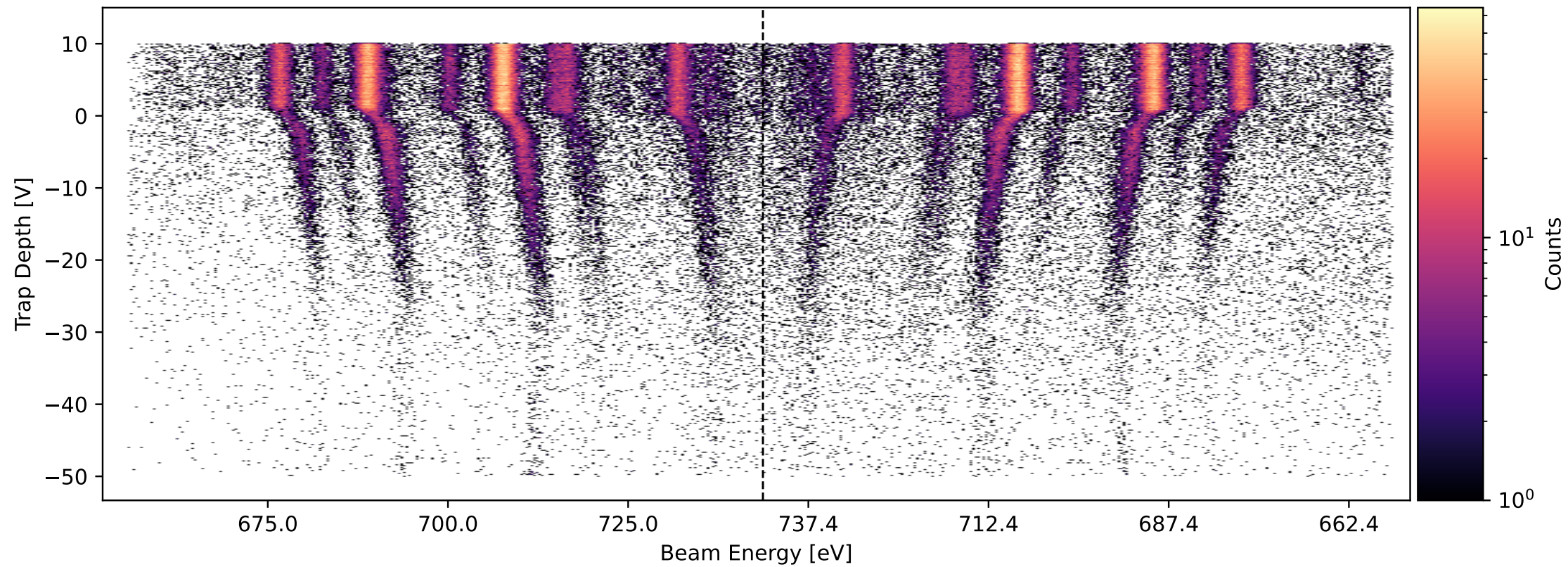
Neon KLL Resonances at an Electron Beam Current of 1.06 mA
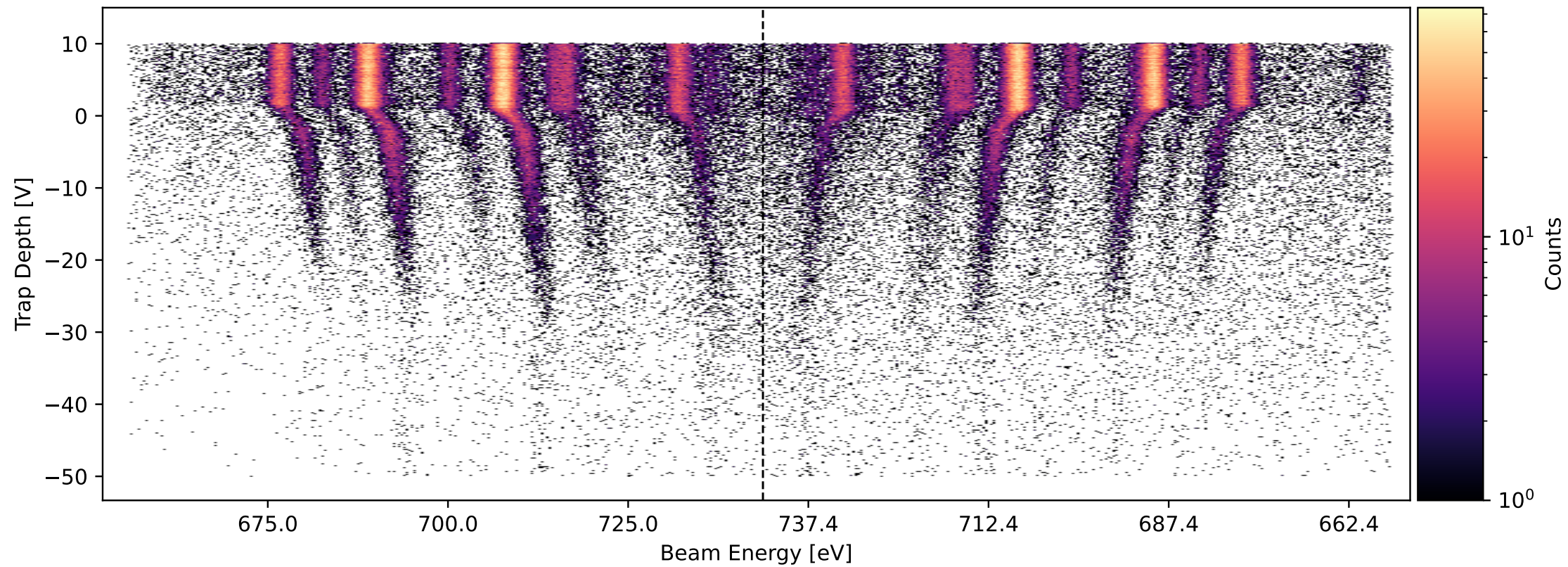
Neon KLL Resonances at an Electron Beam Current of 1.14 mA
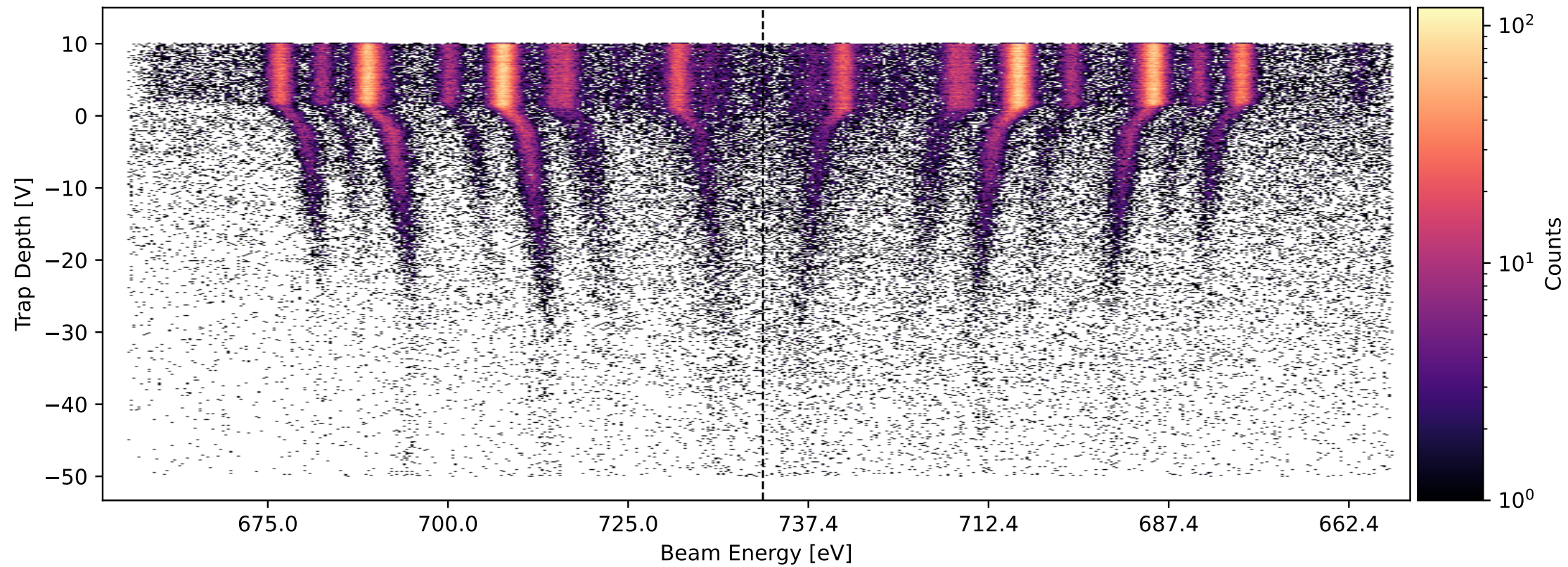
Neon KLL Resonances at an Electron Beam Current of 1.21 mA
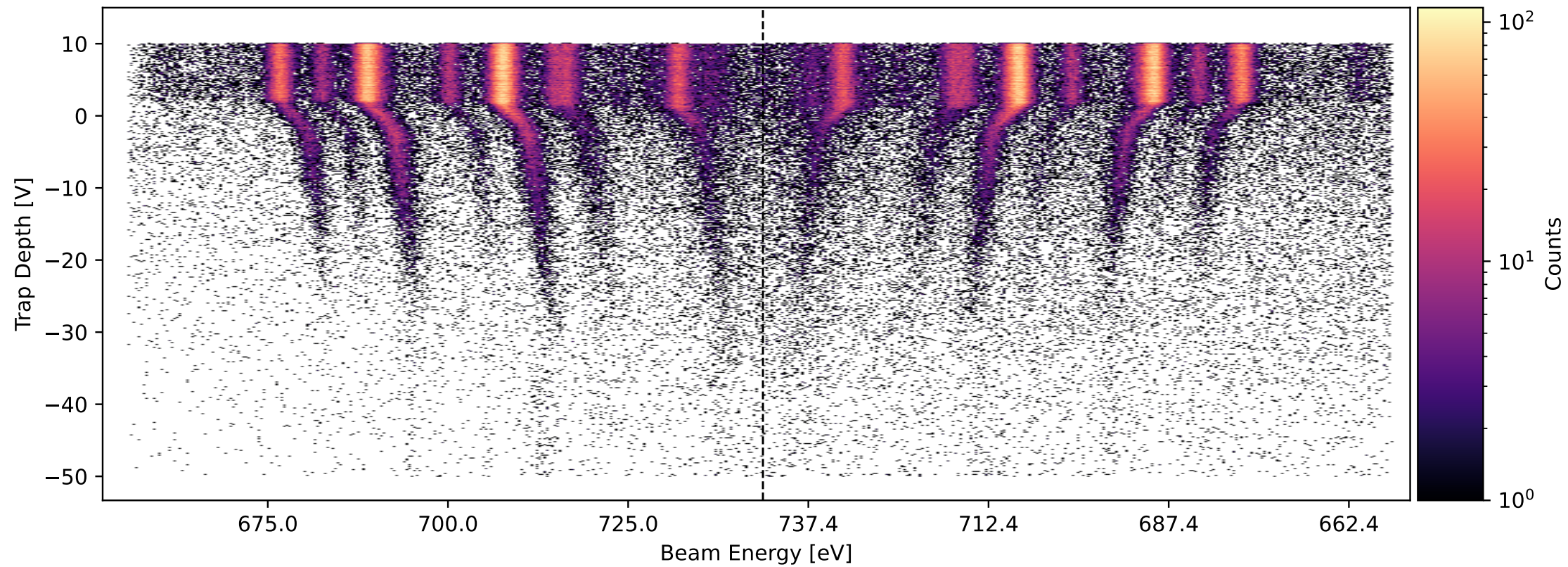
Neon KLL Resonances at an Electron Beam Current of 1.29 mA
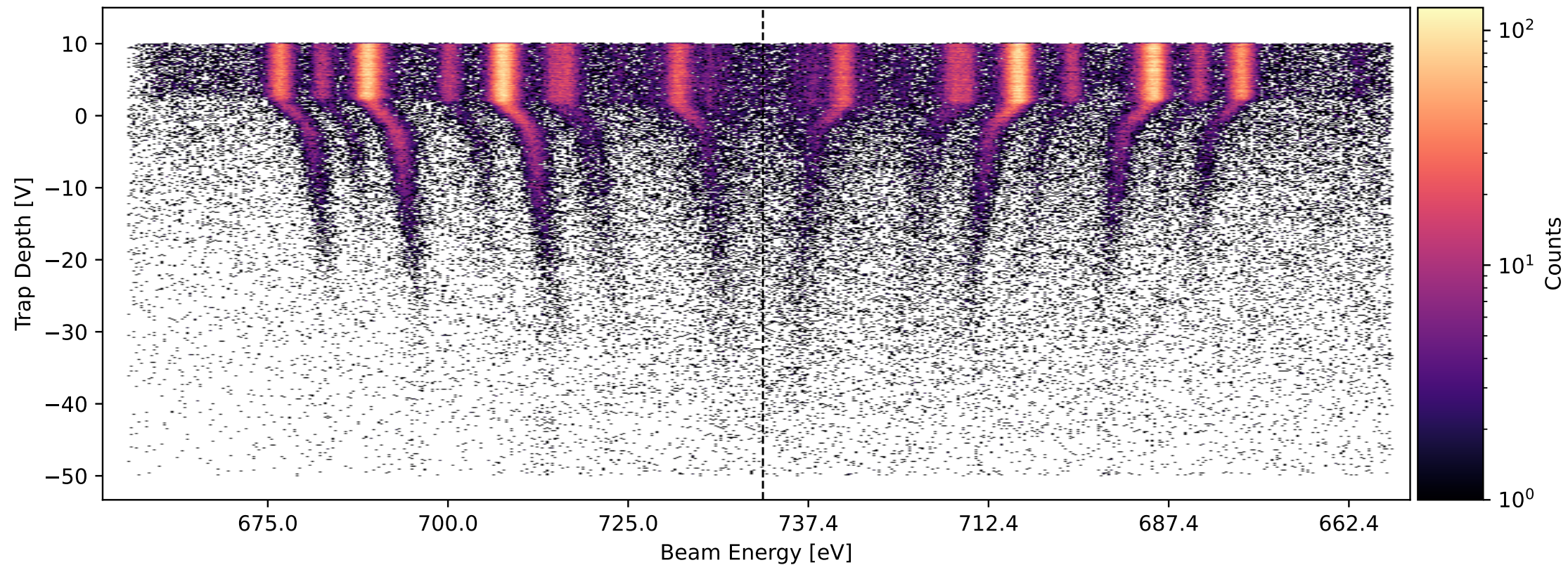
Neon KLL Resonances at an Electron Beam Current of 1.37 mA

Neon KLL Resonances at an Electron Beam Current of 1.45 mA

Neon KLL Resonances at an Electron Beam Current of 1.53 mA

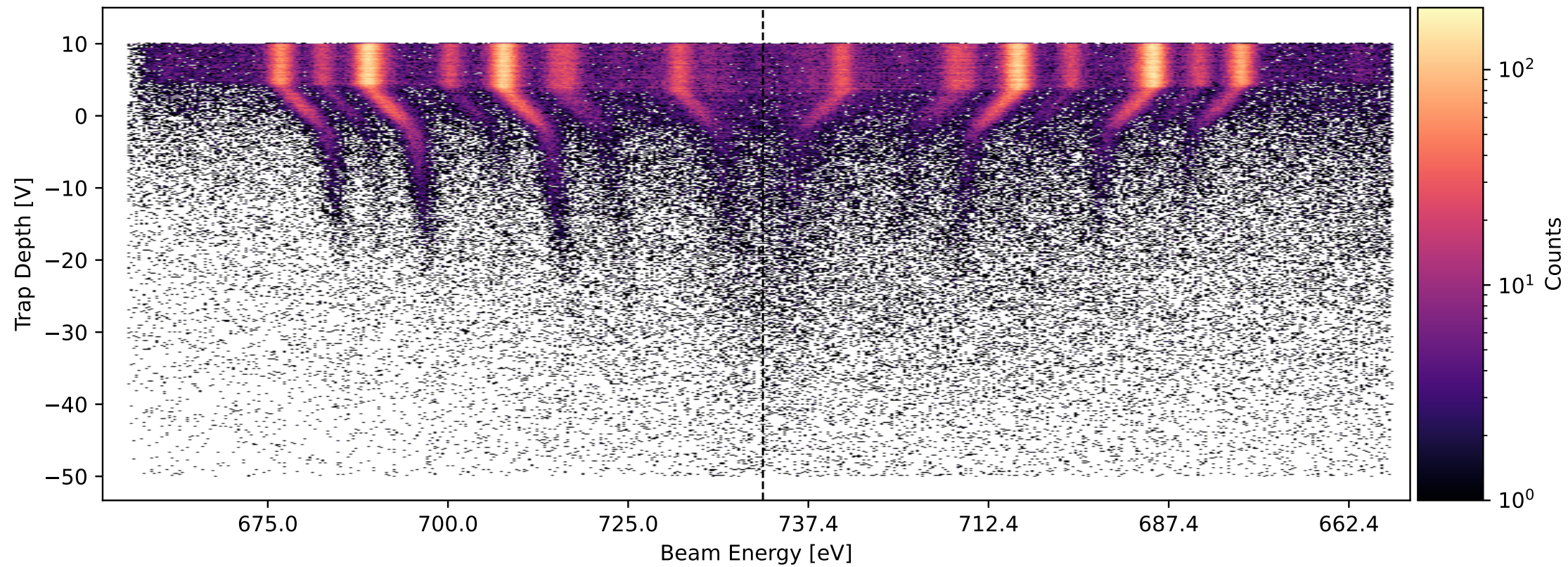Neon KLL Resonances at an Electron Beam Current of 1.6 mA

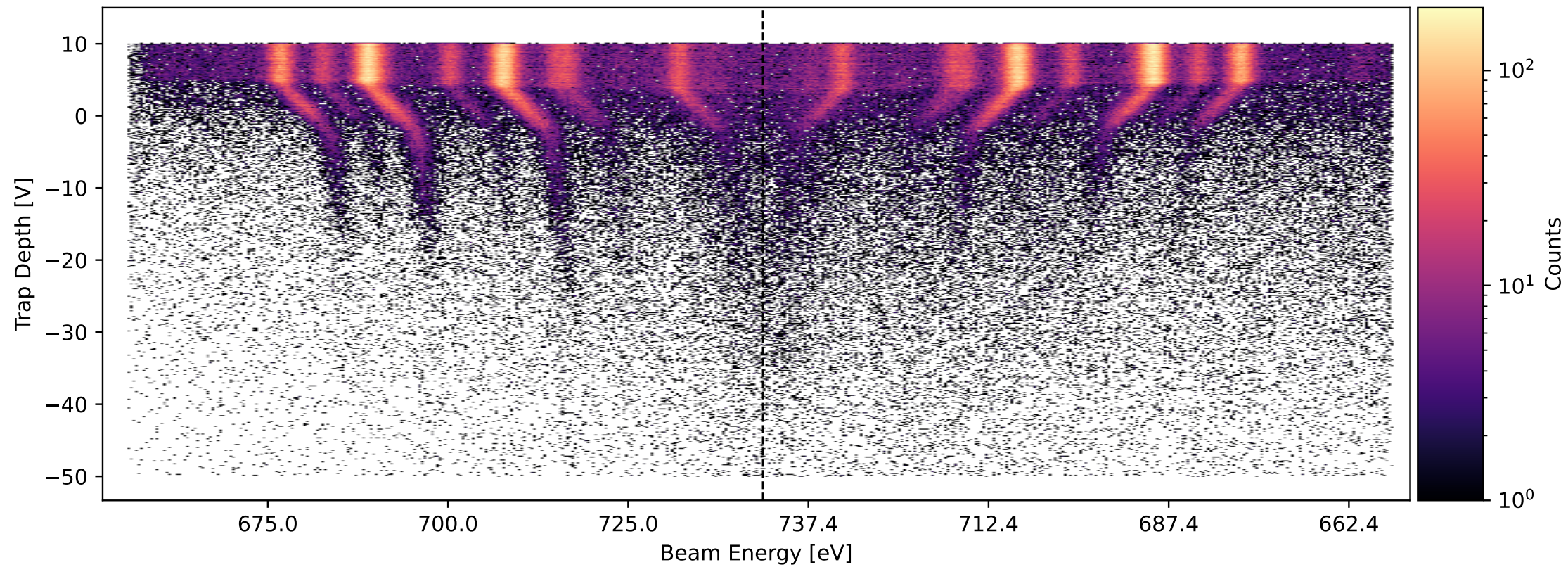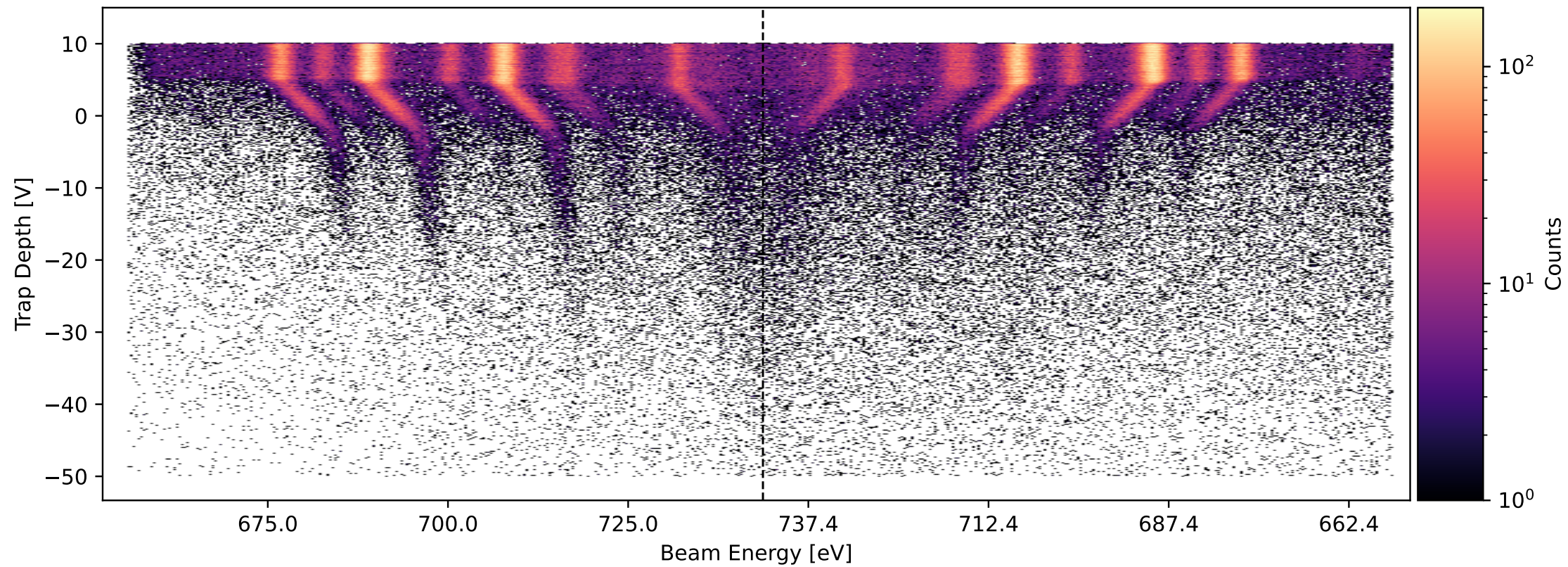Neon KLL Resonances at an Electron Beam Current of 1.69 mA

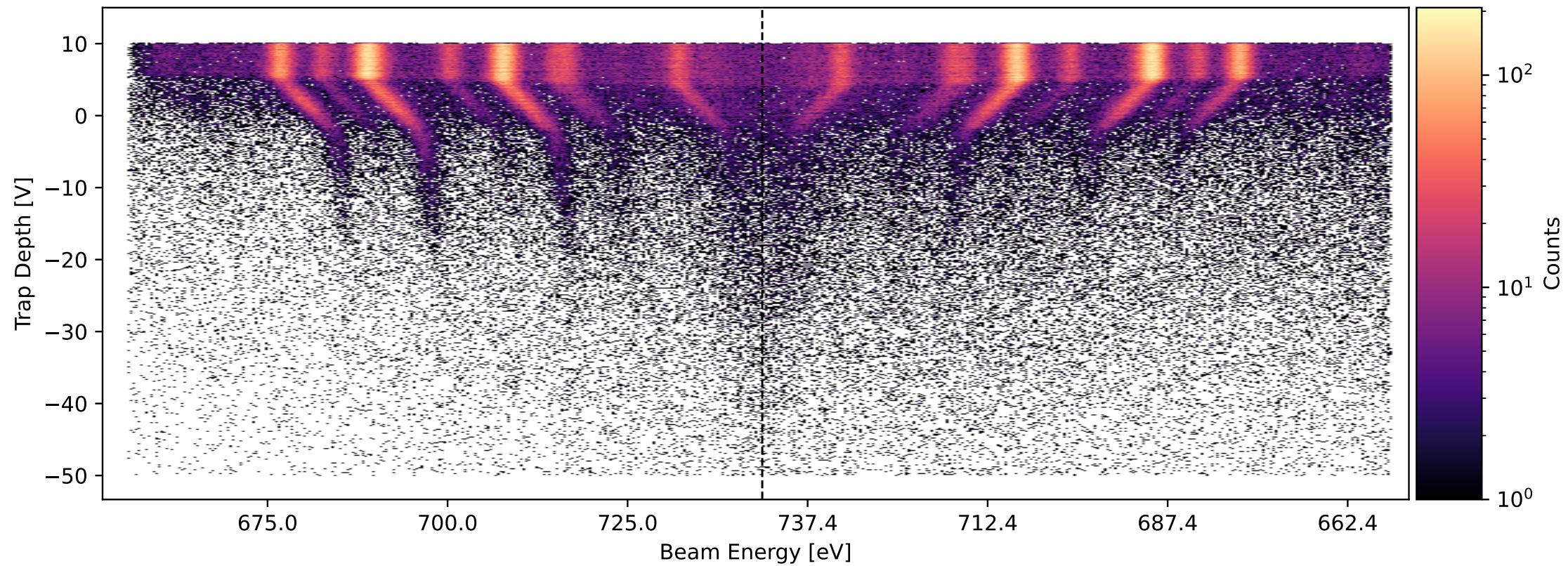Neon KLL Resonances at an Electron Beam Current of 1.77 mA

Neon KLL Resonances at an Electron Beam Current of 1.85 mA

Neon KLL Resonances at an Electron Beam Current of 1.93 mA

Neon KLL Resonances at an Electron Beam Current of 2.01 mA

Bibliography

[1] T. P. Arthanayaka et al. "Measurements of the effective electron density in an electron beam ion trap using extreme ultraviolet spectra and optical imaging". In: *Review of Scientific Instruments* 89.10 (2018), 10E119. DOI: 10.1063/1.5036758. eprint: https://doi.org/10.1063/1.5036758. URL: https://doi.org/10.1063/1.5036758.

[2] Lisa Buchauer. "Konstruktion einer kompakten Elektronenstrahl-Ionenfalle mit Permanentmagneten für Fluoreszenzmessungen". deu. bachelor. Heidelberg: Ruprecht-Karls-Universität, 2012.

[3] Fred Currell and Gerd Fußmann. "Physics of electron beam ion traps and sources". In: *Plasma Science, IEEE Transactions on* 33 (Jan. 2006), pp. 1763–1777. DOI: 10.1109/TPS.2005.860072.

[4] Stepan Dobrodey. "Untersuchung von K-LL-Resonanzen dielektronischer Rekombination und simultaner Innerschalen-Vakuum-Ultraviolett Übergänge in hochgeladenem Eisen mit einer Elektronenstrahl- Ionenfalle". deu. MA thesis. Heidelberg: Ruprecht-Karls-Universität, 2014.

[5] M F Gu. "The flexible atomic code". In: *Canadian Journal of Physics* 86.5 (2008), pp. 675–689. DOI: 10.1139/p07-197. eprint: https://doi.org/10.1139/p07-197. URL: https://doi.org/10.1139/p07-197.

[6] *H150 VITUS X-ray Silicon Drift Detector Product Information.* https://www.ketek.net/wp-content/uploads/2017/01/KETEK_VITUS_H150_Product_Information.pdf. Accessed: 9.8.2021.

[7] Z. Harman. "Theoretical data for KLL dielectronic recombination resonances". In: (May 2011).

[8] D. A. Knapp et al. "Observation of Interference between Dielectronic Recombination and Radiative Recombination in Highly Charged Uranium Ions". In: *Phys. Rev. Lett.* 74 (1 Jan. 1995), pp. 54–57. DOI: 10.1103/PhysRevLett.74.54. URL: https://link.aps.org/doi/10.1103/PhysRevLett.74.54.

[9] A. E. Kramida and M.-C. Buchet-Poulizac. "Energy levels and spectral lines of Ne VII". In: *The European Physical Journal D - Atomic, Molecular, Optical and Plasma Physics* 38.2 (May 2006), pp. 265–276. ISSN: 1434-6079. DOI: `10.1140/epjd/e2006-00025-3`. URL: `https://doi.org/10.1140/epjd/e2006-00025-3`.

[10] A. E. Kramida and M.-C. Buchet-Poulizac. "Energy levels and spectral lines of Ne VIII". In: *The European Physical Journal D - Atomic, Molecular, Optical and Plasma Physics* 39.2 (Aug. 2006), pp. 173–188. ISSN: 1434-6079. DOI: `10.1140/epjd/e2006-00122-3`. URL: `https://doi.org/10.1140/epjd/e2006-00122-3`.

[11] G. Y. Liang et al. "EXPERIMENTAL INVESTIGATIONS OF ION CHARGE DISTRIBUTIONS, EFFECTIVE ELECTRON DENSITIES, AND ELECTRON-ION CLOUD OVERLAP IN ELECTRON BEAM ION TRAP PLASMA USING EXTREME-ULTRAVIOLET SPECTROSCOPY". In: *The Astrophysical Journal* 702.2 (Aug. 2009), pp. 838–850. DOI: `10.1088/0004-637x/702/2/838`. URL: `https://doi.org/10.1088/0004-637x/702/2/838`.

[12] P. Micke et al. "The Heidelberg compact electron beam ion traps". In: *Review of Scientific Instruments* 89.6 (2018), p. 063109. DOI: `10.1063/1.5026961`. eprint: `https://doi.org/10.1063/1.5026961`. URL: `https://doi.org/10.1063/1.5026961`.

[13] Nobuyuki Nakamura. "Breit interaction effect on dielectronic recombination of heavy ions". In: *Journal of Physics B: Atomic, Molecular and Optical Physics* 49.21 (Oct. 2016), p. 212001. DOI: `10.1088/0953-4075/49/21/212001`. URL: `https://doi.org/10.1088/0953-4075/49/21/212001`.

[14] Frederik B.S. Paerels and Steven M. Kahn. "High-Resolution X-Ray Spectroscopy with Chandra and XMM-Newton". In: *Annual Review of Astronomy and Astrophysics* 41.1 (2003), pp. 291–342. DOI: `10.1146/annurev.astro.41.071601.165952`. eprint: `https://doi.org/10.1146/annurev.astro.41.071601.165952`. URL: `https://doi.org/10.1146/annurev.astro.41.071601.165952`.

[15] John Oliver Stoner. *Spectroscopy*. `https://www.britannica.com/science/spectroscopy`. Accessed 5 September 2021. Mar. 2021.

[16] *TREK 677B*. `https://www.advancedenergy.com/globalassets/resources-root/data-sheets/en-hv-amplifier-trek-677b-data-sheet.pdf`. Accessed: 27.8.2021.

[17] B. J. Wargelin, S. M. Kahn, and P. Beiersdorfer. "Dielectronic satellite contributions to Ne VIII and Ne IX K-shell spectra". In: *Phys. Rev. A* 63 (2 Jan. 2001), p. 022710. DOI: 10.1103/PhysRevA.63.022710. URL: https://link.aps.org/doi/10.1103/PhysRevA.63.022710.

[18] K. Yao et al. "KLL dielectronic recombination resonant strengths of He-like up to O-like xenon ions". In: *Phys. Rev. A* 81 (2 Feb. 2010), p. 022714. DOI: 10.1103/PhysRevA.81.022714. URL: https://link.aps.org/doi/10.1103/PhysRevA.81.022714.

Erklärung

Ich versichere, dass ich diese Arbeit selbstständig verfasst und keine anderen als die angegebenen Quellen und Hilfsmittel benutzt habe.

Heidelberg, den 7. September 2021,

(Joschka Goes)